

## Frazil ice growth and production during katabatic wind events in the Ross Sea, Antarctica

1 Lisa Thompson<sup>1,5</sup>, Madison Smith<sup>2</sup>, Jim Thomson<sup>2</sup>, Sharon Stammerjohn<sup>3</sup>, Steve Ackley<sup>4</sup>, and  
2 Brice Loose<sup>5</sup>

3

4 <sup>1</sup>Department of Science, US Coast Guard Academy, New London CT

5 <sup>2</sup>Applied Physics Laboratory, University of Washington, Seattle WA

6 <sup>3</sup>Institute for Arctic and Alpine Research, University of Colorado at Boulder, Boulder CO

7 <sup>4</sup>University of Texas at San Antonio, San Antonio TX

8 <sup>5</sup>Graduate School of Oceanography, University of Rhode Island, Narragansett RI

9

10 *Correspondence to:* Brice Loose (bloose@uri.edu)

11

12 **ABSTRACT:** Katabatic wind in coastal polynyas expose the ocean to extreme heat loss, causing  
13 intense sea ice production and dense water formation around Antarctica throughout autumn and  
14 winter. The advancing sea ice pack, combined with high winds and low temperatures, have  
15 limited surface ocean observations of polynyas in winter, thereby impeding new insights into the  
16 evolution of these ice factories through the dark austral months. Here, we describe oceanic  
17 observations during multiple katabatic wind events during May, 2017 in the Terra Nova Bay and  
18 Ross Sea polynyas. Wind speeds regularly exceeded  $20 \text{ m s}^{-1}$ , air temperatures were below  $-25$   
19  $^{\circ}\text{C}$ , and the oceanic mixed layer extended to 600 meters. During these events, CTD profiles  
20 revealed bulges of warm, salty water directly beneath the ocean surface and extending  
21 downwards tens of meters. These profiles reveal latent heat and salt release during  
22 unconsolidated frazil ice production, driven by atmospheric heat loss, a process that has rarely if  
23 ever been observed outside the laboratory. A simple salt budget suggests these anomalies reflect  
24 in-situ frazil ice concentration that range over from 13 to  $266 \times 10^{-3} \text{ kg m}^{-3}$ . Contemporaneous  
25 estimates of vertical mixing reveal rapid convection in these unstable density profiles, and  
26 mixing lifetimes from 12 to 7 minutes, respectively. The individual estimates of ice production  
27 from the salt budget reveal the intensity of short-term ice production, up to  $110 \text{ cm d}^{-1}$  during the  
28 windiest events, and a seasonal average of  $29 \text{ cm d}^{-1}$ . We further found that frazil ice production  
29 rates covary with wind speed and with location along the upstream-downstream length of the

30 polynya. These measurements reveal that it is possible to indirectly observe and estimate the  
31 process of unconsolidated ice production in polynyas by measuring upper ocean water column  
32 profiles. These vigorous ice production rates suggest frazil ice may be an important component  
33 in total polynya ice production.

34

35

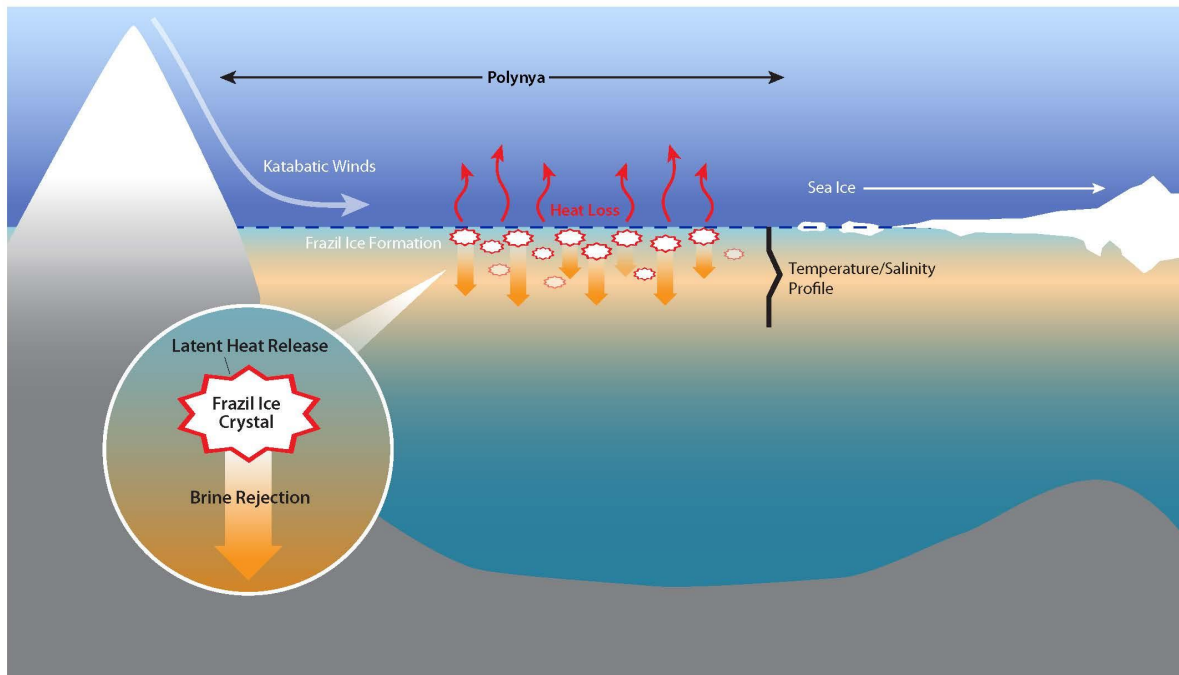
36

## 37 **1. INTRODUCTION**

38

39 Latent heat polynyas form in areas where prevailing winds or oceanic currents create  
40 divergence in the ice cover, leading to openings either surrounded by extensive pack ice or  
41 bounded by land on one side and pack ice on the other (coastal polynyas) (Armstrong, 1972;  
42 Park et al, 2018). The open water of polynyas is critical for air-sea heat exchange, since ice  
43 covered waters are better insulated and reduce the net heat flux to the atmosphere (Fusco et al.,  
44 2009; Talley et al, 2011). A key feature of coastal or latent heat polynyas are katabatic winds  
45 (Figure 1), which form as cold, dense air masses over the ice sheets of Antarctica. These air  
46 masses flow as gravity currents, descending off the glacier, sometimes funneled by topography,  
47 as in the Terra Nova Bay Polynya whose katabatic winds form in the transantarctic mountains.  
48 This episodic offshore wind creates and maintains latent heat polynyas. This study focuses on in-  
49 situ measurements taken from two coastal latent heat polynyas in the Ross Sea, the Terra Nova  
50 Bay and the Ross Sea polynyas.

51



52  
 53 Figure 1: Schematic of a latent heat or coastal polynya. The polynya is kept open by katabatic  
 54 winds which drive sea ice advection, oceanic heat loss and frazil ice formation. Ice formation  
 55 results in oceanic loss of latent heat to the atmosphere and brine rejection. Inset is a schematic of  
 56 frazil ice formation that depicts the release of latent heat of fusion and brine rejection as a frazil  
 57 ice crystal is formed.

58 Extreme oceanic heat loss in polynyas can generate supercooled water (colder than the  
 59 freezing point, Skogseth et al., 2009; Dmitrenko et al, 2010; Matsumura & Ohshima, 2015),  
 60 which is the precursor to ice nucleation. Ice formation begins with fine disc-shaped or dendritic  
 61 crystals called frazil ice, which remain disaggregated when turbulent mixing is vigorous. These  
 62 frazil ice crystals (Figure 1 inset) are about 1 to 4 mm in diameter and 1-100  $\mu\text{m}$  thick (Martin,  
 63 1981). In polynyas, can mix vertically over a region of 5-15 meters depth, while being  
 64 transported downwind from the formation site (Heorton et al, 2017; Ito et al, 2015). Katabatic  
 65 winds sustain the polynya by clearing frazil ice, which piles up at the polynya edge to form a  
 66 consolidated ice cover (Morales Maqueda et al, 2004; Ushio and Wakatsuchi, 1993, Wilchinsky  
 67 et al, 2015).

68 Brine rejection during ice crystal formation (Cox & Weeks, 1983) increases seawater  
 69 salinity and density (Ohshima et al, 2016). In polynyas, this process is episodic and persistent

70 over months, leading to the production of a water mass known as High Salinity Shelf Water  
71 (HSSW) (Talley et al, 2011). In the case of the Ross Sea, HSSW formed on the continental shelf,  
72 is eventually incorporated in Antarctic Bottom Water (AABW) thereby contributing to one of  
73 most abundant water masses (Cosimo & Gordon, 1998; Jacobs, 2004; Martin, et al., 2007;  
74 Tamura et al.; 2008). The Terra Nova Bay polynya produces especially dense HSSW, of  
75 approximately 1-1.5 Sv of HSSW annually (Buffoni et al., 2002; Orsi & Wiederwohl, 2009;  
76 Sansivero et al, 2017; Van Woert 1999a,b).

77 Estimates suggest that as much as 10 % of Antarctic sea ice cover is produced within  
78 coastal polynyas (Tamura et al.; 2008). Given their importance to the seasonal sea ice cycle and  
79 to AABW formation, there is considerable motivation to understand and accurately estimate the  
80 rate of ice production in polynyas. Previous studies by Gallee (1997), Petrelli et al. (2008), Fusco  
81 et al. (2002), and Sansivero et al. (2017) have used models to predict polynya ice production  
82 rates on the order of tens of centimeters per day. Drucker et al (2011), Ohshima et al (2016)  
83 Nihasi and Oshima (2015), and Tamura et al (2016) used satellite-based remote sensing methods  
84 to estimate average annual production rates from 6 to 13 cm d<sup>-1</sup>. In contrast, Schick (2018) and  
85 Kurtz and Bromwich (1985) used heat fluxes to estimate polynya ice production rates, to  
86 produce average rates from 15 to 30 cm d<sup>-1</sup>, revealing apparent offsets in the average production  
87 rate, possibly based on methodology. Sea ice formation is a heterogeneous and disaggregated  
88 process of ice formation, which occurs on small scales of  $\mu\text{m}$  to cm, but accumulates laterally  
89 over km in very harsh observational conditions. These conditions make it difficult to capture  
90 these processes and scales with models and remote estimates, and they render direct  
91 measurements and mechanistic predictions even more challenging (Fusco et al., 2009; Tamura et  
92 al., 2008).

93

## 94 **1.1 Motivation for this article**

95 A set of CTD profiles, measured during late autumn in the Ross Sea coastal polynyas, revealed  
96 anomalous bulges of warmer, saltier water near the ocean surface during katabatic wind events.  
97 During these events, we also observed wind rows of frazil ice aggregation, suggesting that the  
98 CTD profiles were recording salt and heat accumulation during in-situ frazil ice formation – a  
99 process that has rarely been observed outside the lab, let alone in such a vigorously mixed  
100 environment. This study attempts to validate and confirm these observations and presents

101 supporting evidence from coincident observations of air temperature, wind speed, and surface  
102 sea state (§2). We use inventory of excess salt to estimate frazil ice concentration in the water  
103 column (§4). To better understand the importance of frazil formation process, we compute the  
104 lifetime of the salinity anomalies (§5) and we infer a frazil ice production rate (§6). Lastly, we  
105 attempt to scale up the production rate to a seasonal average, while keeping in mind the  
106 complications associated with spatial variability of ice production and the negative feedback  
107 between ice cover and frazil ice formation.

108

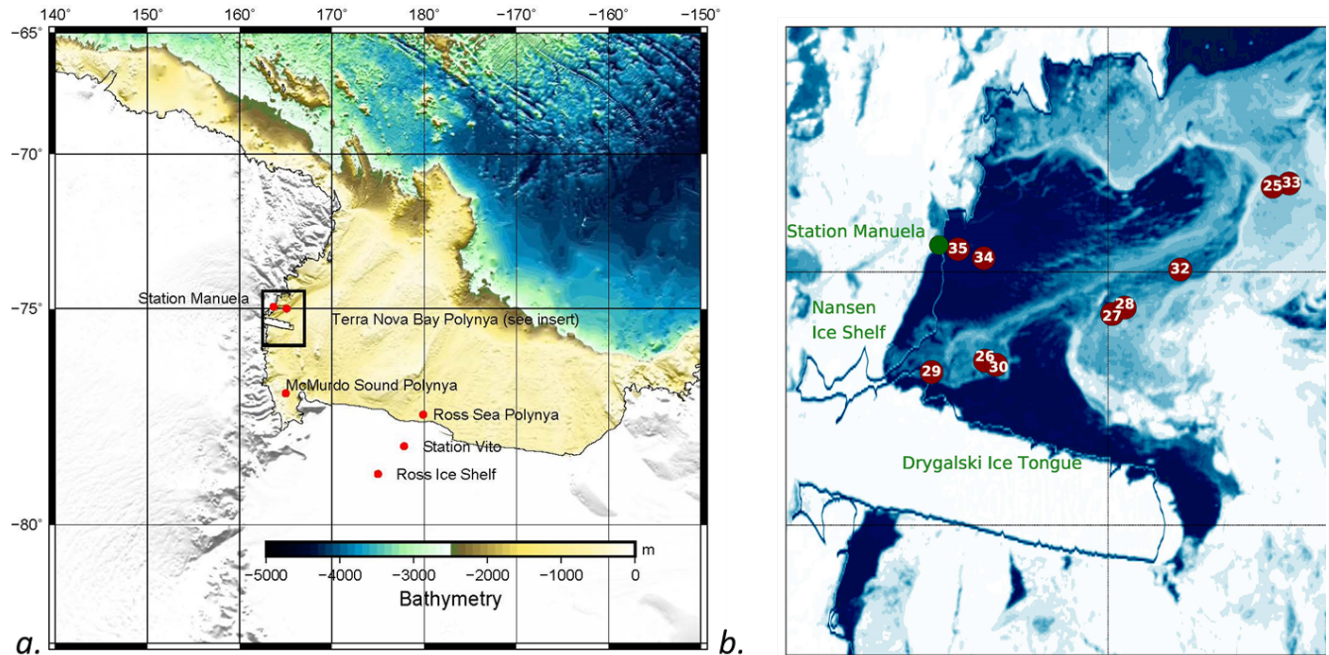
## 109 **2. STUDY AREA AND DATA**

110

### 111 **2.1 The Terra Nova Bay Polynya and Ross Sea Polynya**

112 The Ross Sea, a southern extension of the Pacific Ocean, abuts Antarctica along the  
113 Transantarctic Mountains and has three recurring latent heat polynyas: Ross Sea polynya (RSP),  
114 Terra Nova Bay polynya (TNBP), and McMurdo Sound polynya (MSP) (Martin et al., 2007).  
115 The RSP is Antarctica's largest recurring polynya, the average area of the RSP is 27,000 km<sup>2</sup> but  
116 can grow as large as 50,000 km<sup>2</sup> depending on environmental conditions (Morales Maqueda, et  
117 al., 2004; Park et al, 2018). It is located in the central and western Ross Sea to the east of Ross  
118 Island, adjacent to the Ross Ice Shelf (Figure 2), and typically extends the entire length of the  
119 Ross Ice Shelf (Martin et al., 2007; Morales Maqueda et al., 2004). TNBP is bounded to the  
120 south by the Drygalski ice tongue, which serves to control the polynya maximum size (Petrelli et  
121 al., 2008). TNBP and MSP, the smallest of the three polynyas, are both located in the western  
122 Ross Sea (Figure 2). The area of TNBP, on average is 1300 km<sup>2</sup>, but can extend up to 5000 km<sup>2</sup>;  
123 the oscillation period of TNBP broadening and contracting is 15-20 days (Bromwich & Kurtz,  
124 1984). During the autumn and winter season, Morales Maqueda et al., (2004) estimated TNBP  
125 cumulative ice production to be around 40-60 meters of ice per season, or approximately 10% of  
126 the annual sea ice production that occurs on the Ross Sea continental shelf. The RSP has a lower  
127 daily ice production rate, but produces three to six times as much as TNBP annually due to its  
128 much larger size (Petrelli et al., 2008).

129



130  
 131 Figure 2: Map of the Ross Sea and the Terra Nova Bay Polynya. a) Overview of the Ross Sea,  
 132 Antarctica highlighting the locations of the three recurring polynyas: Ross Sea Polynya (RSP),  
 133 Terra Nova Bay Polynya (TNBP), and McMurdo Sound Polynya (MSP). Bathymetry source:  
 134 GEBCO 1-degree grid. b) Terra Nova Bay Polynya Insert as indicated by black box in panel a.  
 135 MODIS image of TNBP with the 10 CTD stations with anomalies shown. Not included is CTD  
 136 Station 40, the one station with an anomaly located in the RSP. (CTD Station 40 is represented  
 137 on Figure 2a as the location of the Ross Sea Polynya.) Date of MODIS image is March 13,  
 138 2017; MODIS from during cruise dates could not be used due to the lack of daylight and high  
 139 cloud cover.

140  
 141 **2.2 PIPERS Expedition**

142 The water column measurements took place in late autumn, from April 11 to June 14,  
 143 2017 aboard the RVIB Nathaniel B. Palmer (NB Palmer, NBP17-04) as part of the Polynyas and  
 144 Ice Production in the Ross Sea (PIPERS) program. More information about the research  
 145 activities during the PIPERS expedition is available at  
 146 <http://www.utsa.edu/signl/pipers/index.html>. Vertical profiles of Conductivity, Temperature, and  
 147 Depth (CTD) were taken at 58 stations within the Ross Sea. For the purposes of this study, we  
 148 focus on the 13 stations (CTD 23-35) that occurred within the TNBP and 4 stations (CTD 37-40)

149 within the RSP during katabatic wind events (Figure 2). In total, 11 of these 17 polynya stations  
150 will be selected for use in our analysis, as described in §3.1. CTD station numbers follow the  
151 original enumeration used during NBP17-04, so they are more easily traceable to the public  
152 repository, which is archived as described below in the Data Availability section.

153

### 154 **2.3 CTD measurements**

155 The CTD profiles were carried out using a Seabird 911 CTD (SBE 911) attached to a 24  
156 bottle CTD rosette, which is supported and maintained by the Antarctic Support Contract (ASC).  
157 Between CTD casts, the SBE911 was stored at room temperature to avoid freezing components.  
158 Before each cast, the CTD was soaked at approximately 10 meters for 3-6 minutes until the  
159 spikes in the conductivity readings ceased, suggesting the pump had purged all air bubbles from  
160 the conductivity cell. Each CTD cast contains both down and up cast profiles. In many instances,  
161 the upcast recorded a similar thermal and haline anomaly. However, the 24 bottle CTD rosette  
162 package creates a large wake that disturbs the readings on the up cast leading to some profiles  
163 with missing data points and more smoothed profiles, so only the wake uncontaminated down  
164 casts are used in this analysis (Supplemental Figure 1 offers a comparison of the up vs down  
165 casts).

166 The instrument resolution is critical for this analysis, because the anomalous profiles  
167 were identified by comparing the near surface CTD measurements with other values within the  
168 same profile. The reported initial accuracy for the SBE 911 is  $\pm 0.0003 \text{ S m}^{-1}$ ,  $\pm 0.001 \text{ }^\circ\text{C}$ , and  
169 0.015% of the full-scale range of pressure for conductivity, temperature, and depth respectively.  
170 Independent of the accuracy stated above, the SBE 911 can resolve differences in conductivity,  
171 temperature, and pressure on the order of  $0.00004 \text{ S m}^{-1}$ ,  $0.0002 \text{ }^\circ\text{C}$  and 0.001% of the full range,  
172 respectively (SeaBird Scientific, 2018). The SBE 911 samples at 24 Hz with an e-folding time  
173 response of 0.05 seconds for conductivity and temperature. The time response for pressure is  
174 0.015 seconds.

175 The SBE 911 data were processed using post-cruise calibrations by Sea-Bird Scientific.  
176 Profiles were bin-averaged at two size intervals: one-meter depth bins and 0.1-meter depth bins,  
177 to compare whether bin averaging influenced the heat and salt budgets. We observed no  
178 systematic difference between the budget calculations derived from one-meter vs 0.1-meter bins;  
179 the results using one-meter bins are presented in this publication. All thermodynamic properties

180 of seawater were evaluated via the Gibbs Seawater toolbox, which uses the International  
181 Thermodynamic Equation of Seawater – 2010 (TEOS-10). All temperature measurements are  
182 reported as enthalpy conserving or “conservative” temperature; all salinity measurements are  
183 reported as absolute salinity in  $\text{g kg}^{-1}$ . It should be noted that the freezing point calculation can  
184 vary slightly, depending on the choice of empirical relationships that are used (e.g. TEOS-10 vs.  
185 EOS-80, Nelson et al., 2017).

186

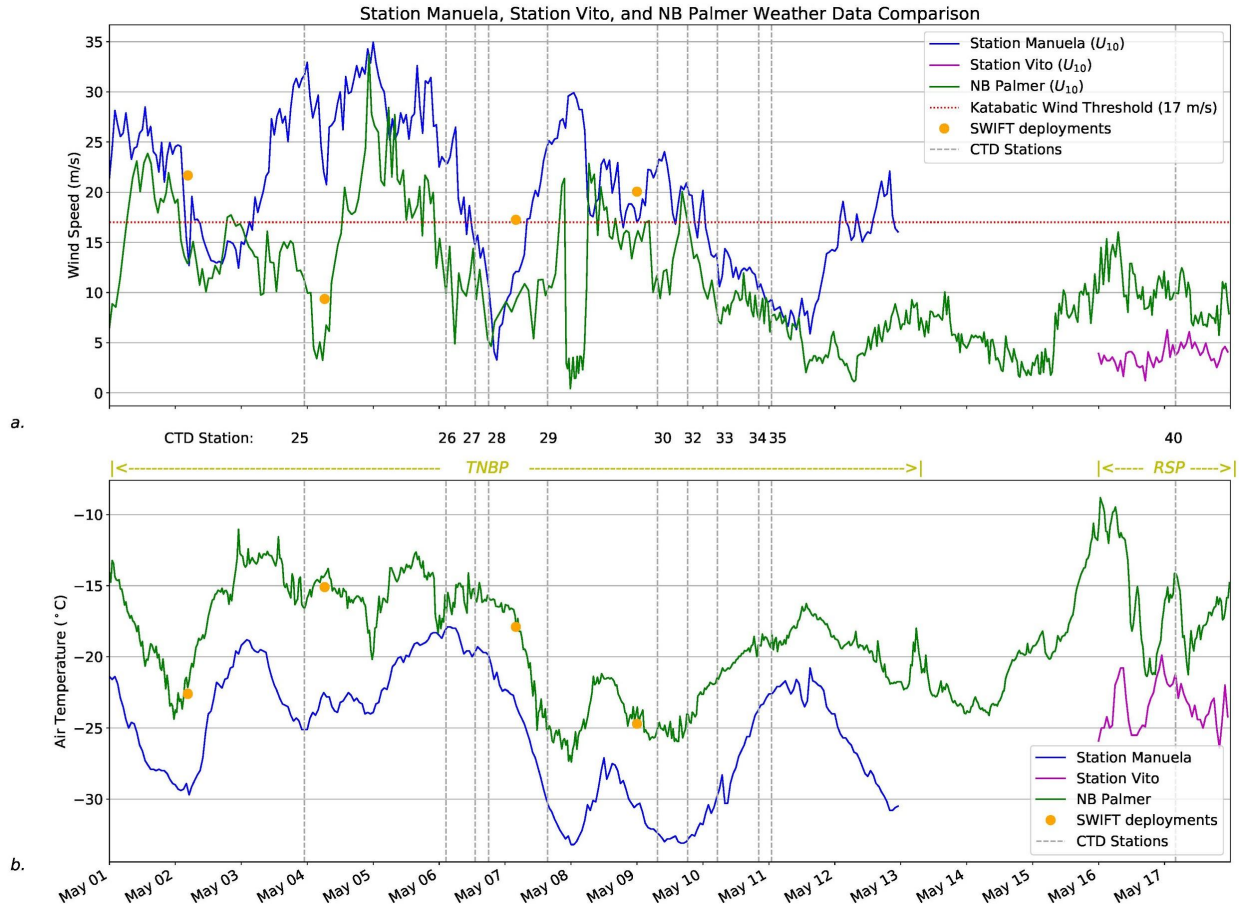
## 187 **2.4 Weather observations**

188 Air temperature and wind speed were measured at the NB Palmer meteorological mast,  
189 and from the automatic weather Station Manuela, on Inexpressible Island, and Station Vito, on  
190 the Ross Ice Shelf (Figure 2a). Observations from all three were normalized to a height of 10  
191 meters using the logarithmic wind profile (Figure 3). The NB Palmer was in TNB from May 1  
192 through May 13, and in the RSP from May 16-18. During both periods, the shipboard air  
193 temperature was consistently warmer than the temperature measured at Stations Manuela and  
194 Vito (Figure 3). Wind speed measured at Station Manuela was consistently higher than shipboard  
195 wind speed, but wind at Station Vito was slightly less than what was observed in the RSP aboard  
196 NB Palmer. At Station Manuela (TNBP) the winds are channelized and intensified through  
197 adjacent steep mountain valleys, the winds at Station Vito (RSP) are coming off the Ross Ice  
198 Shelf. This may explain the differences in wind speed.

199 During the CTD sampling in the TNBP there were 4 periods of intense katabatic wind  
200 events, with each event lasting for at least 24 hours or longer. During the CTD sampling in the  
201 RSP there was just one event of near katabatic winds ( $> 10 \text{ ms}^{-1}$ ) lasting about 24 hours. During  
202 each wind event, the air temperature oscillated in a similar pattern and ranged from  
203 approximately  $-10 \text{ }^{\circ}\text{C}$  to  $-30 \text{ }^{\circ}\text{C}$ .

204





205

206 Figure 3: Weather observations from 01 May to 17 May 2017. a.) Wind speed from Station  
 207 Manuela (blue line), Station Vito (purple line), NB Palmer (green line), and SWIFT (orange  
 208 marker) deployments adjusted to 10 meters. The commonly used katabatic threshold of  $17 \text{ m s}^{-1}$   
 209 is depicted as a “dotted red line”, as well as the date and start time of each CTD cast. b) Air  
 210 temperature from Station Manuela, Station Vito, NB Palmer, and SWIFT deployments.

211

### 212 3. EVIDENCE OF FRAZIL ICE FORMATION

213

#### 214 3.1 Selection of profiles

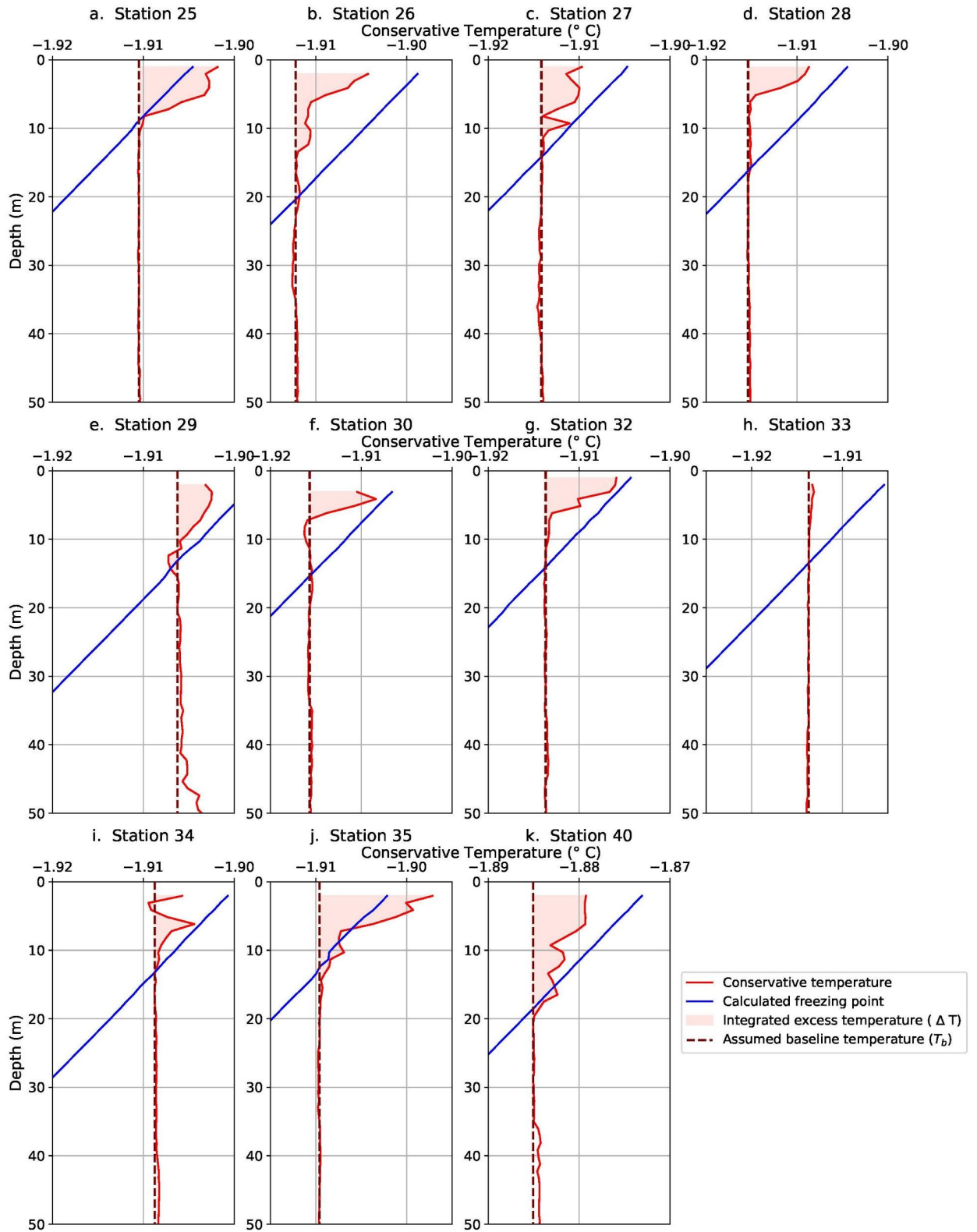
215

216 We used the following selection criteria to identify profiles from the two polynyas that  
 217 appeared to show frazil ice formation: (1) a deep mixed layer extending several hundred meters  
 218 (Supplemental Figure 2), (2) in-situ temperature readings below the freezing point in the near-  
 219 surface water (upper five meters), and (3) an anomalous bolus of warm and/or salty water within

220 the top twenty meters of the profile (Figure 4 and 5). For context, all temperature profiles  
221 acquired during PIPERS (with the exception of one profile acquired well north of the Ross Sea  
222 continental shelf area at 60°S, 170°E) were plotted to show how polynya profiles compared to  
223 those outside of polynyas (Supplemental Figure 2).

224

225



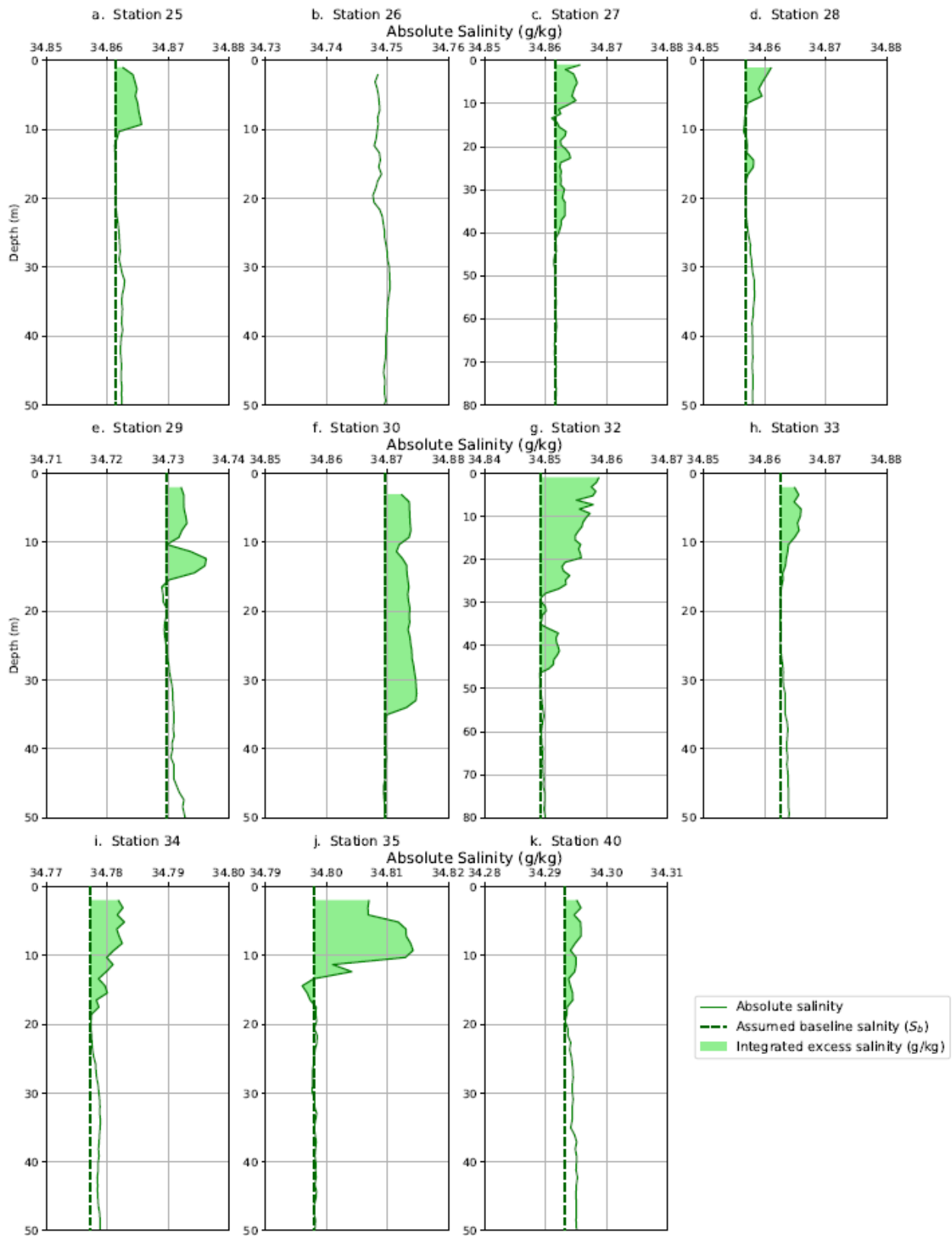
226

227 Figure 4: Conservative Temperature profiles from CTD down casts from 11 stations showing  
 228 temperature and/or salinity anomalies. Plots (a-g) and (j-k) all show an anomalous temperature

229 bulge. They also show supercooled water at the surface with the exceptions of (a) and (j). All of  
230 the plots have an x-axis representing a 0.02 °C change. Profiles (a-j) are from TNBP, and (k) is  
231 from RSP.

232 Polynya temperature profiles were then evaluated over the top 50 meters of the water  
233 column using criteria 2 and 3. Nine TNBP profiles and one RSP profile exhibited excess  
234 temperature anomalies over the top 10-20 m and near-surface temperatures close to the freezing  
235 point (Figure 4). Excess salinity anomalies (Figure 5) were observed at the same stations with  
236 two exceptions: Station 26 had a measurable temperature anomaly (Figure 4b) but no discernible  
237 salinity anomaly (Figure 5b), and Station 33 had a measurable salinity anomaly (Figure 5h) but  
238 no discernible temperature anomaly (Figure 4h). The stations of interest are listed in Table 1.

239



241 Figure 5: Absolute Salinity profiles from CTD down casts from 11 stations showing temperature  
242 and/or salinity anomalies. Profiles (a) and (c-k) show an anomalous salinity bulge in the top 10-  
243 20 meters. Two profiles (c and g) show salinity anomalies extending below 40 meters, so the plot  
244 was extended down to 80 meters to best highlight those. All of the plots (a-k) have an absolute  
245 salinity range of  $0.03 \text{ g kg}^{-1}$ .

246

247

### 248 **3.2 Evaluating the uncertainty in the temperature and salinity anomalies**

249

250 We compared the magnitude of each thermal and haline anomaly to the reported accuracy  
251 of the SBE 911 temperature and conductivity sensors:  $\pm 0.001 \text{ }^\circ\text{C}$  and  $\pm 0.0003 \text{ S m}^{-1}$ , or  
252  $\pm 0.00170 \text{ g kg}^{-1}$  when converted to absolute salinity. To quantify the magnitude of the  
253 temperature anomaly, we computed a baseline excursion,  $\Delta T = T_{\text{obs}} - T_{\text{b}}$ , throughout the anomaly  
254 where  $T_{\text{obs}}$  is the observed temperature at that depth, and  $T_{\text{b}}$  is the in-situ baseline temperature,  
255 which is extrapolated from the far field temperature within the well-mixed layer below the  
256 anomaly (see Figure 4 for schematic). The largest baseline excursion from each of the 11  
257 anomalous CTD profiles, averaged together, yields a value of  $\Delta T = 0.0064 \text{ }^\circ\text{C}$ . While this is a  
258 small absolute change in temperature, it is still 32 times larger than the stated precision of the  
259 SBE 911 ( $0.0002 \text{ }^\circ\text{C}$ ). The same approach was applied to the salinity anomalies yielded an  
260 average baseline excursion of  $0.0041 \text{ S m}^{-1}$  (or  $0.0058 \text{ g kg}^{-1}$  for absolute salinity), which is 100  
261 times larger than the instrument precision ( $0.00004 \text{ S m}^{-1}$ ). Table 1 lists the maximum  
262 temperature and salinity anomalies for each CTD station.

263 The immersion of instruments into supercooled water can lead to a number of unintended  
264 outcomes as instrument surfaces may provide ice nucleation sites, or otherwise perturb an  
265 unstable equilibrium. Robinson et al (2020) highlight a number of the potential pitfalls. One  
266 concern was that ingested frazil ice crystals could interfere with the conductivity sensor. Crystals  
267 smaller than 5 mm can enter the conductivity cell, creating spikes in the raw conductance data.  
268 Additionally, frazil crystals smaller than  $100 \text{ }\mu\text{m}$  would be small enough to pass between the  
269 conductivity electrodes and decrease the resistance/conductance that is reported by the  
270 instrument (Skogseth et al, 2009; Robinson et al, 2020). To test for ice crystal interference, the  
271 raw (unfiltered with no bin averaging) salinity profile was plotted and compared with the 1-meter

272 binned data for the 11 anomalous CTD Stations (Supplemental Figure 3). The raw data showed  
273 varying levels of noise as well as some spikes or excursions to lower levels of conductance; these  
274 spikes may have been due to ice crystal interference. Overall, the bin-averaged profile does not  
275 appear to be biased or otherwise influenced by the spikes, which tend to fall symmetrically  
276 around a baseline. This was demonstrated by bin-averaging over different depth intervals as  
277 described in §2.4. It is also worth pointing out that the effect of these conductivity spikes would  
278 be to decrease the bin-averaged salinity, thereby working against the overall observation of a  
279 positive baseline excursion. In other words, the entrainment of frazil crystals could lead to an  
280 underestimate of the positive salinity anomaly, rather than the production of positive salinity  
281 aberration.

282 Another pitfall highlighted by Robinson et al (2020) is the potential for self-heating of the  
283 thermistor by residual heat in the instrument housing. The results from that study reveal a  
284 thermal inertia that dissipates over a period of minutes. We examined the temperature trace  
285 during the CTD soak and did not observe the same behavior. It is likely that some thermal inertia  
286 did exist at the time of deployment, but any residual heat appeared to dissipate very quickly,  
287 compared to the 3-6 minute soak time before each profile. We suggest the self-heating might be  
288 a problem that arose in a single instrument but is not necessarily diagnostic of all SBE 911  
289 instruments. Robinson et al (2020) did not document this behavior in multiple instruments.  
290 Lastly, the potential for ice formation on the surface of the conductivity cell seems unlikely  
291 because it was kept warm until it was deployed in the water.

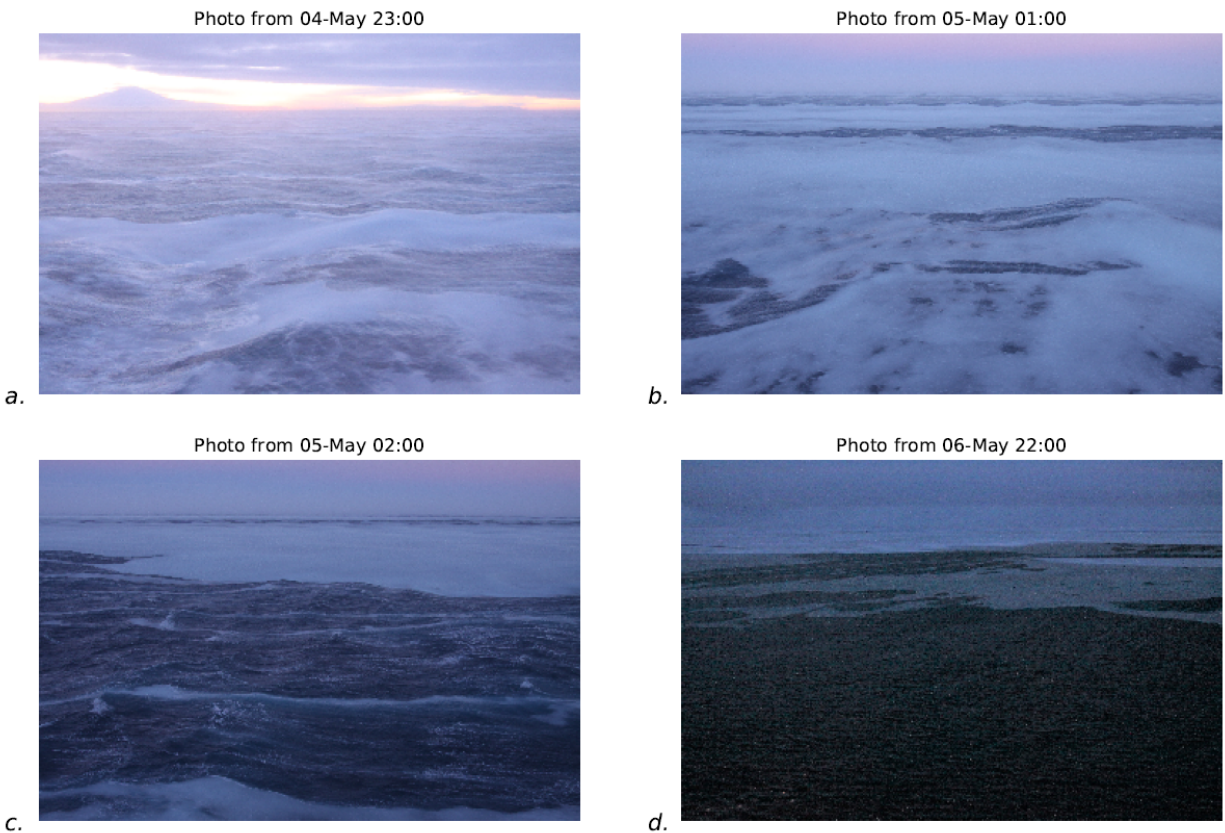
292 The observation of both warm and salty anomalies cannot easily be explained by these  
293 documented instrument biases. A cold instrument might be experience freezing inside the  
294 conductivity cell, but this freezing would not influence the thermistor, which is physically  
295 separated from the conductivity cell. A warm instrument might have contained residual thermal  
296 inertia, which could melt individual frazil ice crystals, but these would produce negative baseline  
297 excursions in salinity, rather than a positive anomaly. The positive anomalies in temperature and  
298 salinity are not easily explained by these instrumental effects.

299

### 300 **3.3 Camera observations of frazil ice formation**

301 During PIPERS an EISCam (Evaluative Imagery Support Camera, version 2) was  
302 operating in time lapse mode, recording photos of the ocean surface from the bridge of the ship

303 every 10 minutes (for more information on the EISCam see Weissling et al, 2009). The images  
304 from the time in TNBP and RSP reveal long streaks and large aggregations of frazil ice. A  
305 selection of photos from TNBP were captured (Figure 6). The winds were strong enough at all  
306 times to advect frazil ice, creating downstream frazil streaks, and eventually pancake ice in most  
307 situations. Smaller frazil streaks and a curtain of frazil ice below the frazil streak were also  
308 visible.  
309



310  
311 Figure 6: Images from NB Palmer as EISCam (Evaluative Imagery Support Camera) version 2.  
312 White areas in the water are loosely consolidated frazil ice crystals being actively formed during  
313 a katabatic wind event. Image (d) was brightened to allow for better contrast.

### 314 315 **3.4 Conditions for frazil ice formation**

316 Laboratory experiments can provide a descriptive picture of the conditions that lead to  
317 frazil ice formation; these conditions are diagnostic of conditions in the TNBP. Ushio and  
318 Wakatsuchi (1993) exposed a 2 x 0.4 x 0.6 m<sup>3</sup> tank to air temperatures of -10 °C and wind



319 speeds of  $6 \text{ m s}^{-1}$ . They observed 0.1 to 0.2 °C of supercooling at the water surface and found  
320 that after 20 minutes the rate of supercooling slowed due to the release of latent heat, coinciding  
321 with visual observation of frazil ice formation. After ten minutes of ice formation, they observed  
322 a measurable increase in temperature of the frazil ice layer of 0.07 °C warmer and 0.5 to 1.0 g  
323  $\text{kg}^{-1}$  saltier, as a consequence of latent heat and salt release during freezing (Ushio and  
324 Wakatsuchi, 1993).

325         In this study, we found the frazil ice layer to be on average 0.006 °C warmer than the  
326 underlying water. Similarly, the salinity anomaly was on average 0.006 g  $\text{kg}^{-1}$  saltier than the  
327 water below. While the anomalies we observed are smaller than those observed in the lab tank by  
328 Ushio and Wakatsuchi (1993), the trend of super-cooling, followed by frazil ice formation and  
329 the appearance of a salinity anomaly is analogous. The difference in magnitude can likely be  
330 explained by the reservoir size; the small volume of the lab tank will retain the salinity and  
331 temperature anomaly, rather than mixing it to deeper depths.

332         Considering the aggregate of supporting information, we infer that the anomalous profiles  
333 from TNBP and RSP were produced by frazil ice formation. The strong winds and sub-zero air  
334 temperatures (§2.4), reveal that conditions were sufficient for frazil formation, similar to the  
335 conditions observed in the laboratory. We showed that the CTD profiles in both temperature and  
336 salinity are reproducible and large enough to be distinguished from the instrument uncertainty  
337 (§3.1 and 3.2). Finally, the EISCam imagery reveals the accumulation of frazil ice crystals at the  
338 ocean surface.

339

340

#### 341 **4. ESTIMATION OF FRAZIL ICE CONCENTRATION USING CTD PROFILES**

342

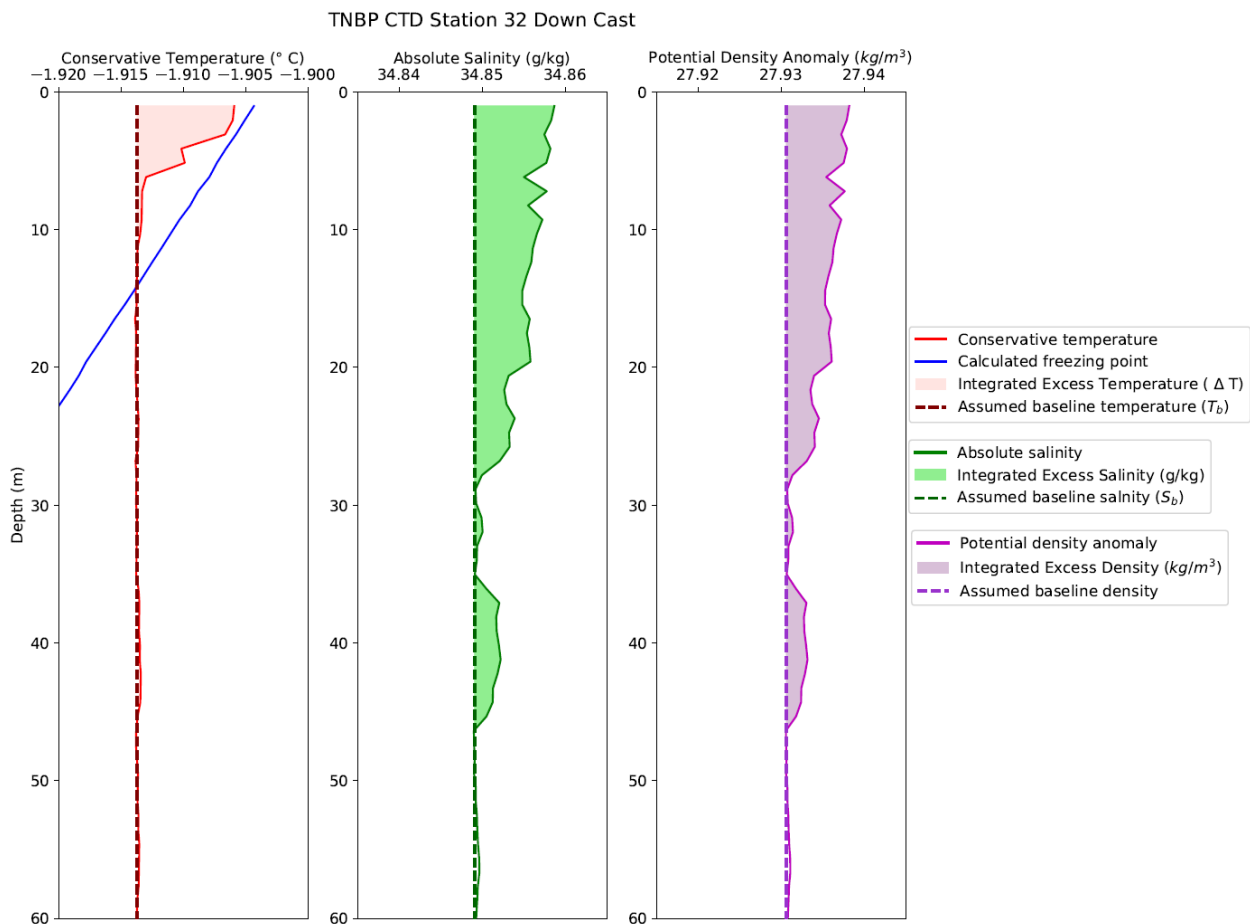
343         Having identified CTD profiles that trace frazil ice formation, we want to know how  
344 much frazil ice can be inferred from these T and S profiles. The inventories of heat and salt from  
345 each profile can provide independent estimates of frazil ice concentration. To simplify the  
346 inventory computations, we neglect the horizontal advection of heat and salt; this is akin to  
347 assuming that lateral variations are not important because the neighboring water parcels are also  
348 experiencing the same intense vertical gradients in heat and salt. We first describe the  
349 computation using temperature in § 4.1 and the computation using salinity in § 4.2.

350

#### 351 4.1 Estimation of frazil ice concentration using temperature anomalies

352 Using the latent heat of fusion as a proxy for frazil ice production we estimated the  
353 amount of frazil ice that must be formed in order to create the observed temperature anomalies.  
354 We estimated the excess enthalpy using the same temperature baseline excursion:  $\Delta T = T_{\text{obs}} - T_b$ ,  
355 defined in §3.2 . The excess over the baseline is graphically represented in Figure 7a. Lacking  
356 multiple profiles at the same location, we are not able to observe the time evolution of these  
357 anomalies, so  $T_b$  represents the best inference of the temperature of the water column prior to the  
358 onset of ice formation; it is highlighted in Figure 7a with the dashed line. The value of  $T_b$  was  
359 determined by averaging the profile temperature over a 10 m interval directly beneath the  
360 anomaly. In most cases, this interval was nearly isothermal and isohaline, as would be expected  
361 within a well-mixed layer. The uncertainty in the value of  $T_b$  was estimated from the standard  
362 deviation within this 10 m interval; the average was  $7.5 \times 10^{-5} \text{ }^\circ\text{C}$ .

363



365 Figure 7: Conservative temperature, absolute salinity, and potential density anomaly for TNBP  
 366 CTD Station 32, May 9, 2017. a) Conservative temperature profile showing the temperature  
 367 anomaly, the selected baseline temperature (dashed line) and the integrated excess temperature  
 368 (shaded area). b) Absolute salinity profile showing the salinity anomaly, the selected baseline  
 369 salinity (dashed line), and integrated excess salinity (shaded area). c) Potential density anomaly  
 370 showing the selected baseline density (dashed) and the excess density instability (shaded).  
 371

372 To find the excess heat ( $Q_{excess}^{total}$ ) contained within the thermal anomaly, we computed the  
 373 vertical integral of heat per unit area from the surface ( $z=0$ ) to the bottom of the anomaly ( $z=z_T$ ):

$$374 \quad Q_{excess}^{total} = \int_{z=0}^{z=z_T} \rho C_p^W \Delta T dz \quad (1)$$

375 Here  $\rho$  is density of seawater,  $z$  is the depth range of the anomaly, and  $C_p^W$  is the specific heat  
 376 capacity ( $C_p^W = 3988 \text{ J kg}^{-1}\text{K}^{-1}$  for TNBP ;  $C_p^W = 3991 \text{ J kg}^{-1}\text{K}^{-1}$  for RSP) . The  
 377 concentration of frazil ice is estimated by applying the latent heat of formation ( $L_f = 330 \text{ kJ kg}^{-1}$ )  
 378 as a conversion factor to  $Q_{excess}^{total}$  :

$$379 \quad C_{ice}^T = \frac{Q_{excess}^{total}}{L_f \cdot z_T} \quad (2)$$

380 The concentration of ice derived represents the total concentration of ice, in  $\text{kg m}^{-3}$ . A more  
 381 detailed explanation of equations (1) and (2) is contained in Supplemental 1. The mass  
 382 concentration of ice derived from the temperature anomaly for each station is listed in Table 1.  
 383

#### 384 **4.2 Estimation of frazil ice concentration using salinity anomalies**

385 The mass of salt within the salinity anomaly was also used to estimate ice formation.  
 386 Assuming that frazil ice crystals do not retain any brine and assuming there is negligible  
 387 evaporation, the salinity anomaly is directly proportional to the ice formed. By using the  
 388 conservation equations for water and salt, the mass of frazil ice can be estimated by comparing  
 389 the excess salt (measured as salinity) with the amount of salt initially present in the profile,  
 390 similar to the inventory for heat. The complete derivation can be found in Supplemental 2. The  
 391 salinity anomaly ( $\Delta S$ ) above the baseline salinity ( $S_b$ ) is  $\Delta S = S_{obs} - S_b$ , and is shown in  
 392 Figure 7b. The initial value of salinity ( $S_b$ ) was established by observing the trend in the salinity  
 393 profile directly below the haline bulge; in most cases the salinity trend was nearly linear beneath  
 394 the bulge, however in general the salinity profiles were less homogeneous than the temperature

395 profiles. As with temperature, we determined  $S_b$  by averaging over a 10 m interval, starting  
396 below the anomaly. The uncertainty in the value of  $S_b$  was estimated from the standard deviation  
397 within this 10 m interval; the average was  $2.8 \times 10^{-4}$ .

398 To find the total mass of frazil ice ( $M_{ice}^S$ ,  $\text{kg m}^{-2}$ ) in the water column, the integral is  
399 taken the salt ratio times the mass of water ( $M_W^O = \rho_b dz$ , where  $\rho_b$  is the assumed baseline  
400 density, or  $1028 \text{ kg m}^{-3}$ ). The concentration of ice ( $C_{ice}^S$ ,  $\text{kg m}^{-3}$ ) is found by dividing the mass of  
401 frazil ice by the depth of the salinity anomaly ( $z_s$ ). The resulting estimates of ice concentration  
402 are listed in Table 1.

$$403 \quad M_{ice}^S = \rho_b \int_{z=0}^{z=z_s} \frac{\Delta S}{S_{obs}} dz \quad (3)$$

$$404 \quad C_{ice}^S = \frac{M_{ice}^S}{z_s} \quad (4)$$

405 A more detailed explanation of equations (3) and (4) is contained in Supplemental 2 and 3.

406

### 407 **4.3 Summary of the frazil ice estimates**

408 The salt inventories yielded frazil ice concentrations from  $13 \times 10^{-3} \text{ kg m}^{-3}$  to  $266 \times 10^{-3}$   
409  $\text{kg m}^{-3}$ , whereas the inventories based on heat range from 8 to  $25 \times 10^{-3} \text{ kg m}^{-3}$  (Table 1). Within  
410 every profile the frazil ice concentration from the salinity inventory exceeds the concentration  
411 derived the heat inventories, suggesting there is a systematic difference between the two. This  
412 difference can most likely be explained by loss of heat from the anomaly to the atmosphere. The  
413 same ocean heat loss that drives frazil ice production can also diminish the latent heat anomaly  
414 as it is produced. There is no corresponding loss term for the salt inventory. By the same token, it  
415 is worth noting that seawater evaporation may yield a small gain to the salt inventory. However,  
416 water vapor pressure is relatively small at these low air temperatures, and evaporative heat loss is  
417 a small term. Mathiot et al. (2012) found that evaporation had a small effect on salinity increases,  
418 when compared to ice production and contributed  $< 4\%$  to salt flux. In the TNBP, the Palmer  
419 meteorological tower revealed high relative humidity (on average 78.3%), which indicates that  
420 there is likely some evaporation that would reduce the mass of ice derived from the salinity  
421 anomaly by small ( $< 4\%$ ) margin. Taken together, these results suggest that the ice  
422 concentrations, derived from the heat anomalies, underestimate frazil ice concentration in  
423 comparison to the salt inventory; the salt inventory may overestimate the ice production, but the  
424 evaporation effect is minimal.

425 Table 1: CTD Stations with temperature and salinity anomalies (see Figures 4-5), showing  
 426 maximum values of the temperature anomaly, depth range of the temperature anomaly,  
 427 concentration of ice derived from the temperature anomaly (§4.1), as well as the maximum value  
 428 of the salinity anomaly, depth range of salinity anomaly, and concentration of ice derived from  
 429 the salinity anomaly (§4.2).

Station	Date and Time (local)	Maximum $\Delta T$ ( $^{\circ}\text{C}$ )	$z_T$ (m)	$C_{ice}^T$ (kg $\text{m}^{-3}$ )	Maximum $\Delta S$ ( $\text{g kg}^{-1}$ )	$z_S$ (m)	$C_{ice}^S$ (kg $\text{m}^{-3}$ )
25	May 03 23:00:41	0.009	11.34	$48 \times 10^{-3}$	0.004	13.4	$67 \times 10^{-3}$
26*	May 06 02:30:08	0.008	24.73	$14 \times 10^{-3}$	--	--	--
27	May 06 13:08:11	0.005	15.45	$22 \times 10^{-3}$	0.003	41.22	$46 \times 10^{-3}$
28	May 06 17:59:12	0.007	15.52	$18 \times 10^{-3}$	0.004	17.52	$21 \times 10^{-3}$
29	May 07 15:29:32	0.004	11.34	$22 \times 10^{-3}$	0.007	21.64	$51 \times 10^{-3}$
30	May 09 07:28:24	0.007	8.24	$25 \times 10^{-3}$	0.005	36.07	$105 \times 10^{-3}$
32	May 09 18:24:56	0.008	11.33	$32 \times 10^{-3}$	0.007	47.4	$119 \times 10^{-3}$
33**	May 10 05:16:29	---	---	---	0.004	22.67	$29 \times 10^{-3}$
34	May 10 20:16:46	0.004	13.4	$9 \times 10^{-3}$	0.005	19.58	$89 \times 10^{-3}$

35	May 11 00:56:32	0.012	19.58	$35 \times 10^{-3}$	0.016	14.43	$266 \times 10^{-3}$
40	May 17 04:02:37	0.006	20.61	$33 \times 10^{-3}$	0.003	18.55	$13 \times 10^{-3}$

430 \*Station 26 did not have a measurable salinity anomaly but was included due to the clarity of the  
431 temperature anomaly. Conversely, \*\*Station 33 did not have a measurable temperature anomaly  
432 but was included due to the clarity of the salinity anomaly.

433

## 434 5. ESTIMATION OF TIME SCALE OF ICE PRODUCTION

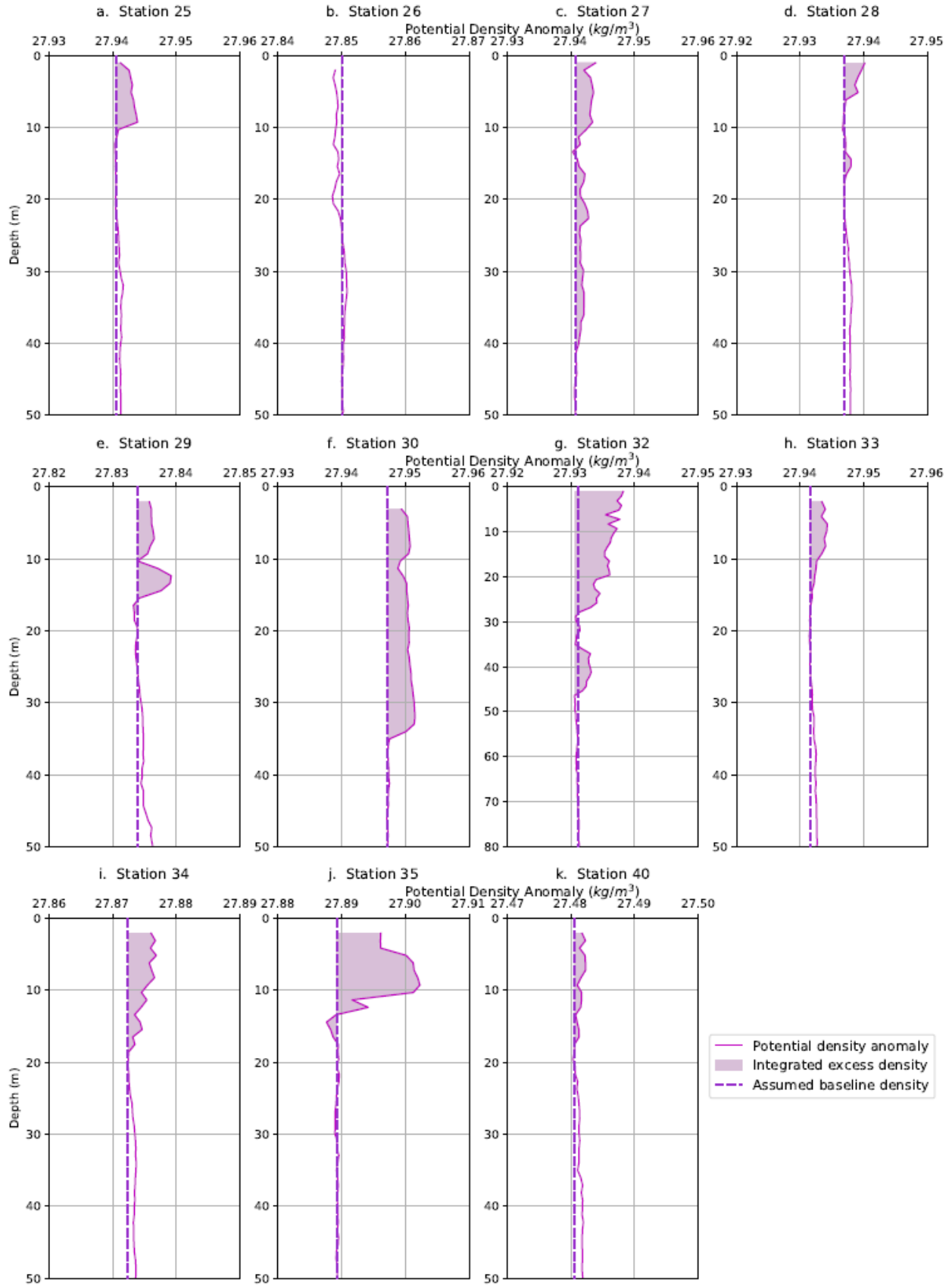
435 To better understand the characteristics of frazil ice production and the resulting water  
436 column signature, we can seek the lifetime of these T and S anomalies. Are they short-lived in  
437 the absence of forcing, or do they represent an accumulation over some longer ice formation  
438 period? One possibility is that the anomalies begin to form at the onset of the katabatic wind  
439 event, implying that the time required to accumulate the observed heat and salt anomalies is  
440 similar to that of a katabatic wind event (e.g. 12-48 hours). This, in turn would suggest that the  
441 estimates of frazil ice concentration have accumulated over the lifetime of the katabatic wind  
442 event. Another interpretation is that the observed anomalies reflect the near-instantaneous  
443 production of frazil ice. In this scenario, heat and salt are simultaneously produced and actively  
444 mixed away into the far field. In this case, the observed temperature and salinity anomalies  
445 reflect the net difference between production and mixing. One way to frame the question of the  
446 anomaly lifetime is to ask “if ice production stopped, how long would it take for the heat and salt  
447 anomalies to dissipate?” The answer depends on how vigorously the water column is mixing. In  
448 this section, we examine the mixing rate. However, we can first get some indication of the  
449 timescale by the density profiles.

450

### 451 5.1 Apparent instabilities in the density profiles

452 The computed density profiles reveal an unstable water column for all but one of our  
453 eleven stations (Figure 8). These suggest that buoyancy production from excess heat did not  
454 effectively offset the buoyancy loss from excess salt within each anomaly. It is not common to

455 directly observe water column instability without the aid of microstructure or other instruments  
456 designed for measuring turbulence.





458 Figure 8: Potential density anomalies for all 11 stations with evidence of active frazil ice  
459 formation. The integrated excess density and assumed baseline density are depicted to highlight  
460 the instability. Note that Station 26 (b) does not present a density anomaly because it does not  
461 have a salinity anomaly. In the absence of excess salinity, the temperature anomaly created  
462 instead an area of less dense water (i.e., a stable anomaly).

463  
464 An instability in the water column that persists long enough to be measured in a CTD  
465 profile, must be the result of a continuous buoyancy loss that is created at a rate faster than it can  
466 be eroded by mixing. In other words, the katabatic winds appeared to dynamically maintain these  
467 unstable profiles. Continuous ice production leads to the production of observed heat and salt  
468 excesses at a rate that exceeds the mixing rate. If the unstable profiles reflect a process of  
469 continuous ice production, then the inventory of ice that we infer from our simple heat and salt  
470 budgets must reflect ice production during a relatively short period of time, defined by the time it  
471 would take to mix the anomalies away, once the wind-driven dynamics and ice production  
472 stopped.

473 Robinson et al (2014) found that brine rejection from platelet ice formation also leads to  
474 dense water formation and a static instability. Frazil ice can form in Ice Shelf Water that is  
475 subjected to adiabatic cooling during its buoyant ascent from beneath the ice shelf. This leads to  
476 a supercooled water mass, ice nucleation, and a stationary instability, which was observable  
477 before being mixed away by convection (Robinson et al, 2014). This process not takes place at  
478 200-300 m water depth, away from the air-sea interface, but it results in a water column  
479 signature that is similar to those observed in this study.

480

## 481 **5.2 Lifetime of the salinity anomalies**

482 To estimate the lifetime of each salinity anomaly requires an estimate of the rate of  
483 turbulent mixing in the mixed layer. The Kolmogorov theory for turbulent energy distribution  
484 defines the eddy turnover time as the time it takes for a parcel to move a certain distance,  $d$ , in a  
485 turbulent flow (Valis, 2017). The smallest eddy scale is that of turbulent energy dissipation, and  
486 the largest scale is bounded by the length of the domain and the free stream turbulent velocity  
487 (Cushman-Roisin, 2019). This timescale can be estimated as

488 
$$t \approx \frac{d}{(\varepsilon d)^{\frac{1}{3}}} \approx \left(\frac{d^2}{\varepsilon}\right)^{\frac{1}{3}}. \quad (5)$$

489 Here,  $d$  is the characteristic length of the largest eddy and  $\varepsilon$  is the turbulent kinetic energy (TKE)  
 490 dissipation rate, which is related to the free stream velocity as  $\varepsilon \sim w^3/d$  (Cushman-Roisin, 2019).  
 491 In this section we discuss and derive the best available estimates  $t$  using measurements of the  
 492 meteorological forcing conditions and in-situ measurements of the turbulence.

493 If  $d$  is bounded only by the domain (in this case, the mixed layer depth), this would  
 494 suggest vertical turbulent eddies up to 600 m in length (Table 2). However, a homogenous  
 495 mixed-layer does not necessarily imply active mixing throughout the layer (Lombardo and  
 496 Gregg, 1989). Instead, the length scale of the domain is more appropriately estimated from the  
 497 size of the buoyancy instability and the background wind shear, or the Monin-Obukhov length  
 498 ( $L_{M-O}$ ) (Monin & Obukhov, 1954). When  $L_{M-O}$  is small and positive, buoyant forces are  
 499 dominant and when  $L_{M-O}$  is large and positive, wind shear forces are dominant (Lombardo &  
 500 Gregg, 1989). The  $L_{M-O}$  is estimated using the salt-driven buoyancy flux, reflecting the same  
 501 process that gave rise to the observed salinity anomalies (see §4.3 for more detail).

502  
 503 
$$L_{M-O} = -\frac{u_*^3}{k\beta gw\overline{\Delta S}}, \quad (6)$$

504  
 505 where  $u_*$  is the aqueous friction velocity,  $g$  is gravitational acceleration,  $w$  is the water vertical  
 506 velocity,  $\overline{\Delta S}$  is the salt flux,  $\beta$  is the coefficient of haline contraction, and  $k$  is the von Karman  
 507 constant. A more detailed explanation, along with the specific values are listed in Supplemental  
 508 4.

509 The friction velocity derives from the wind speed ( $U_P$ ), measured at the NB Palmer  
 510 weather mast from a height of  $z_P = 24$  m, adjusted to a 10 meter reference ( $U_{10}$ ) (Manwell et al.,  
 511 2010).

512  
 513 
$$U_{10} = U_P \frac{\ln\left(\frac{z}{z_0}\right)}{\ln\left(\frac{z_P}{z_0}\right)} \quad (7)$$

514  
 515 Roughness class 0 was used in the calculation and has a roughness length of  $0.2\mu\text{m}$ . These  
 516 values are used to estimate the wind stress as

517  $\tau = C_D \rho_{air} U_{10}^2$ , (8)

518 where  $\rho_{air}$  represents the density of air, with a value of  $1.3 \text{ kg m}^{-3}$  calculated using averages  
 519 from NB Palmer air temperature ( $-18.7 \text{ }^\circ\text{C}$ ), air pressure (979.4 mbars) and relative humidity  
 520 (78.3%).  $C_D$ , the dimensionless drag coefficient, was calculated as  $1.525 \times 10^{-3}$  using the  
 521 NOAA COARE 3 model, modified to incorporate wave height and speed (Fairall et al, 2003).  
 522 The average weather data from NB Palmer was paired with the wave height and wave period  
 523 from the SWIFT deployment (Surface Wave Instrument Float with Tracking) on 04 May to find  
 524  $C_D$ . A more detailed explanation and the specific values are listed in Supplemental 5. Finally,  $u_*$   
 525 from equation (6) is:

526  $u_* = \sqrt{\frac{\tau}{\rho_{water}}}$ . (9)

527 During the katabatic wind events, a buoy was deployed to measure  $\epsilon$ ,  $w$ , and wave field  
 528 properties (Thomson, 2012; Thomson et al, 2016; Zippel & Thomson, 2016). SWIFT  
 529 deployments occurred within the period of CTD observations, as shown in the timeline of events  
 530 (Supplemental Figure 5), however they do not coincide in time and space with the CTD profiles.  
 531 For the vertical velocity estimation, we identified the 04 May and 09 May SWIFT deployments  
 532 as most coincident to CTD stations analyzed here, based on similarity in wind speeds. The  
 533 average wind speed at all the CTD stations with anomalies was  $10.2 \text{ m s}^{-1}$ . For the 04 May  
 534 SWIFT deployment, the wind speed was  $9.36 \text{ m s}^{-1}$ . CTD Station 32 experienced the most  
 535 intense sustained winds of  $18.9 \text{ m s}^{-1}$ . The 09 May SWIFT deployment was applied to CTD 32,  
 536 which had a wind speed of  $20.05 \text{ m s}^{-1}$ . During these SWIFT deployments, 04 May had an  
 537 average value of  $w = 0.015 \text{ m s}^{-1}$  and 09 May had an average value of  $w = 0.025 \text{ m s}^{-1}$ .

538 The TKE dissipation rates are expected to vary with wind speed, wave height, ice  
 539 thickness and concentration (Smith & Thomson, 2019). Wind stress is the source of momentum  
 540 to the upper ocean, but this is modulated by scaling parameter ( $c_e$ , Smith & Thomson, 2019). If  
 541 the input of TKE is in balance with the TKE dissipation rate over an active turbulent layer, the  
 542 following expression can be applied:

543  $c_e \tau \propto \rho \int \epsilon(z) dz$ , (10)

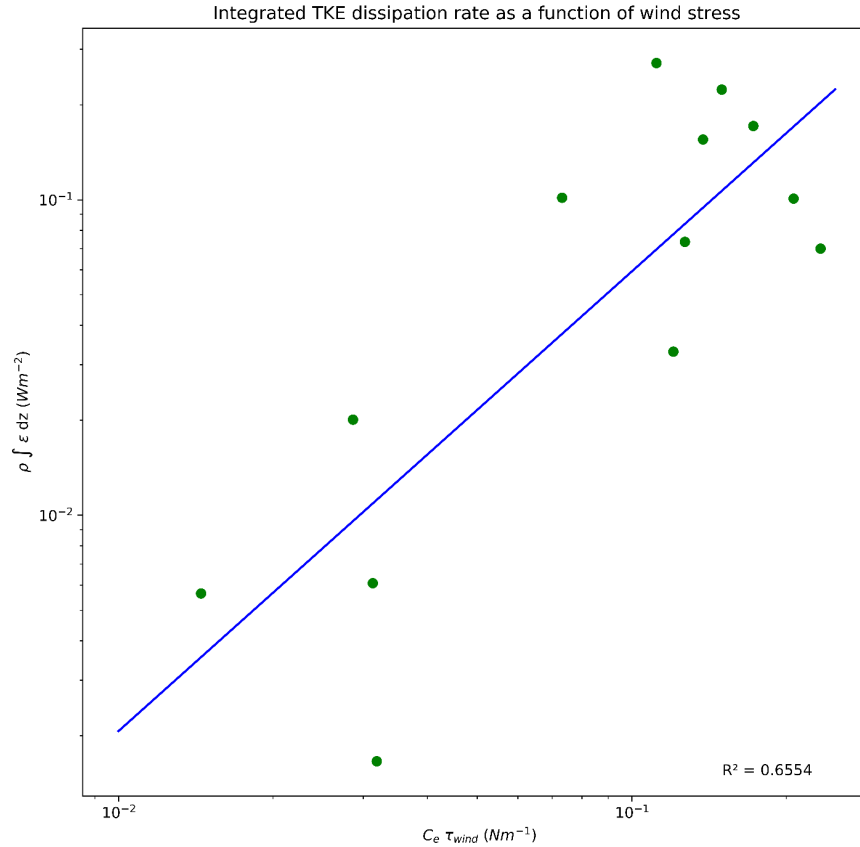
544  
 545 where the density of water ( $\rho$ ) is assumed to be  $1027 \text{ kg m}^{-3}$  for all stations. This scaling  
 546 parameter incorporates both wave and ice conditions; more ice produces more efficient wind

547 energy transfer, while simultaneously damping surface waves, with the effective transfer velocity  
548 in ice, based on the assumption that local wind input and dissipation are balanced Smith &  
549 Thompson (2019) used the following empirical determination of  $c_e$ :

$$550 \quad c_e = a \left( A \frac{z_{ice}}{H_s} \right)^b. \quad (11)$$

551 Here,  $A$  is the fractional ice cover, with a maximum value of 1,  $z_{ice}$  is the thickness of ice, and  $H_s$   
552 is the significant wave height. Using Antarctic Sea ice Processes and Climate or ASPeCt visual  
553 ice observations ([www.aspect.aq](http://www.aspect.aq)) from NB Palmer, the fractional ice cover and thickness of ice  
554 were found at the hour closest to both SWIFT deployments and CTD profiles (Knuth & Ackley,  
555 2006; Ozsoy-Cicek et al., 2009; Worby et al., 2008). SWIFT wave height measurements yielded  
556 an average value of  $H_s = 0.58$  m for May 04, and this value was applied to all the CTD profiles.  
557 To obtain the most robust data set possible, in total, 13 vertical SWIFT profiles from 02 May, 04  
558 May, and 09 May were used to evaluate equation (12) over an active depth range of 0.62 meters.

559 Using the estimates of  $c_e$ ,  $\tau$ , and  $\varepsilon$  from the SWIFT, we parameterized the relationship  
560 between wind stress and  $\varepsilon$  that is reflected in equation (10). A linear fit on a log-log scale ( $y =$   
561  $10^{(1.4572 \log_{10}(x) + 0.2299)}$ ,  $r^2 = 0.6554$ ) was then applied to NB Palmer wind stress data to derive  
562 estimates of  $\varepsilon$  that coincided with the ambient wind conditions during each CTD station (Table  
563 2).



564

565 Figure 9: Vertical integral of  $\epsilon$ , the TKE dissipation rate, estimated from the SWIFT buoy  
 566 deployments, versus estimates of wind-driven TKE inputs into the surface ocean. A linear  
 567 scaling relationship was applied to the log of each property.

568

569 Gathering these estimates of  $w$ ,  $u_*$ , and  $\epsilon$ , we estimate the anomaly lifetime using  
 570 equation (5). Because  $L_{M-O}$  represents the domain length scale, we rewrite equation (5) as:

571 
$$t = \left( \frac{L_{M-O}^2}{\epsilon} \right)^{\frac{1}{3}} \quad . \quad (12)$$

572

573 The values used to estimate  $L_{M-O}$  were computed as follows: haline contraction,  $\beta$ , in  
 574 equation (6) was calculated from Gibbs Seawater toolbox and averaged over the depth range of  
 575 the anomaly. The excess salt,  $\overline{\Delta S}$ , was found using the average value of  $\Delta S$  for each profile  
 576 anomaly. The values of  $L_{M-O}$  range from 6 m to 330 m (Table 2). In general,  $L_{M-O}$  was greater  
 577 than the length of the salinity anomaly but smaller than the mixed layer depth.

578

579 The mixing lifetime of these salinity anomalies ranged from 2 to 12 minutes, but most  
 values cluster near the average of 9 min. The average timescale is similar to the frazil ice lifetime

580 found in Michel (1967). **These lifetimes suggest that frazil ice production and the observed**  
581 **density instabilities would relax to a neutral profile within ten minutes of a diminution in**  
582 **wind forcing.**

583

## 584 6. RATE OF FRAZIL ICE PRODUCTION

585 We can extend the analysis of anomaly lifetime to estimate the frazil ice production rate.  
586 Heuristically, if turbulence production and dissipation are in balance, the lifetime of the anomaly  
587 is equivalent to the time it would take for the anomaly to be dissipated, or *produced*, given the  
588 observed conditions of heat loss to the atmosphere. By that analogy, the sea ice production rate  
589 is,

590

$$591 \quad r_{ice} = \frac{c_{ice}^S z_S}{t \rho_{ice}} \quad (13)$$

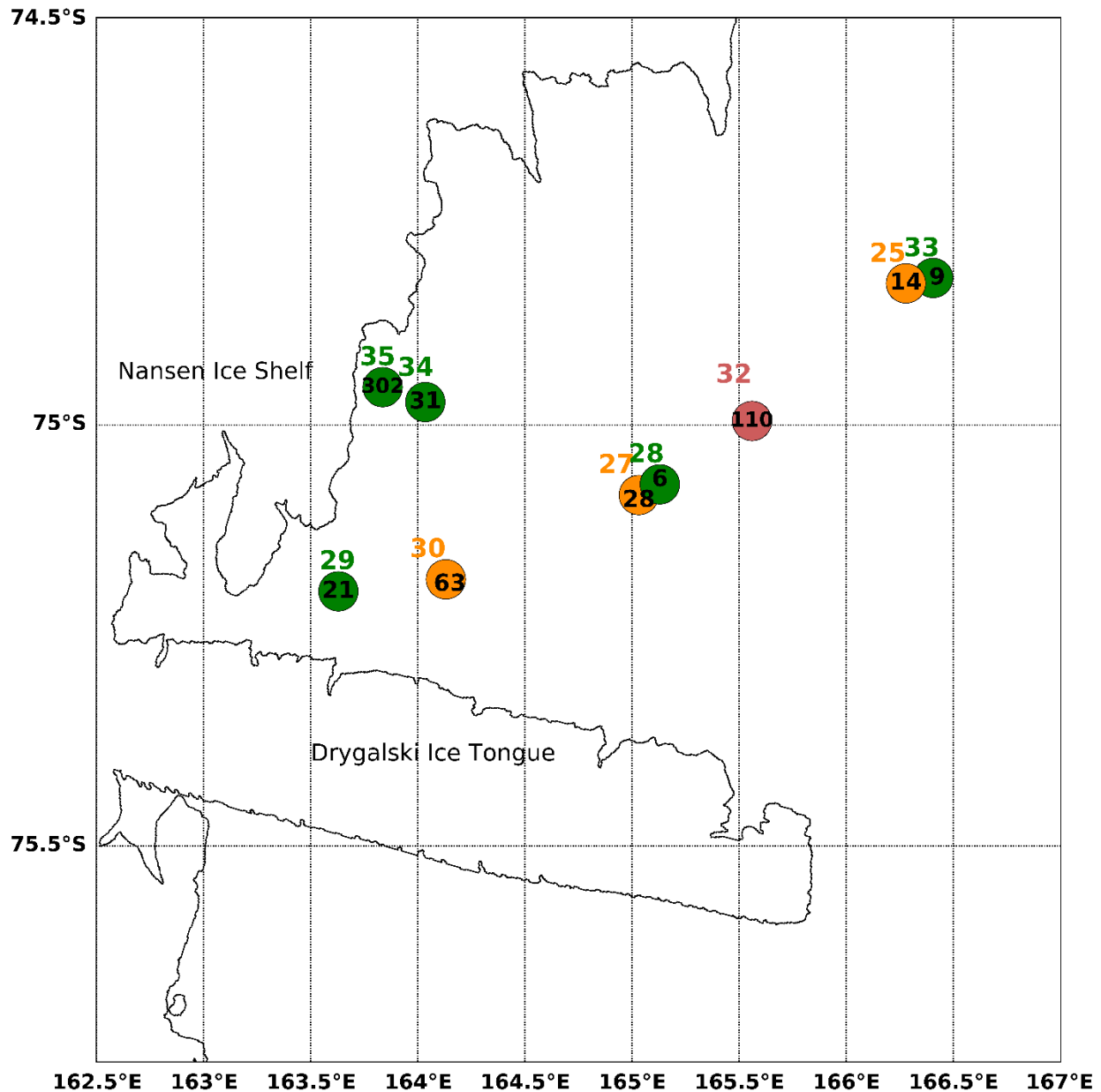
592 Here,  $\rho_{ice} = 920 \text{ kg m}^{-3}$ ; as previously defined,  $z_S$  is the depth of the salinity anomaly in meters.  
593 The results are summarized in Table 2 (see Supplemental 6 for additional detail). To bound the  
594 uncertainty in  $r_{ice}$ , we estimated the 95% confidence interval (CI) for  $\varepsilon$  at each CTD station.  
595 These are expressed as range of ice production rates in Table 2. Uncertainty in the heat and salt  
596 inventories were not included in the uncertainty estimates, because we observed negligible  
597 differences in the inventory while testing the inventory for effects associated with bin averaging  
598 of the CTD profiles (Section 2.3). Another small source of error arises from neglecting  
599 evaporation. To quantify uncertainties introduced by that assumption, we used the bulk  
600 aerodynamic formula for latent heat flux and found the effects of evaporation across the CTD  
601 stations to be 1.8% [0.07-3.45%] (Zhang, 1997). The uncertainty from the effects of evaporation  
602 are similar to Mathiot et al (2012). On average, the lower limit of ice production was 30% below  
603 the estimate and the upper limit was some 44% larger than the estimated production.

604 The estimates of frazil ice production rate span two orders of magnitude, from 3 to 302  
605  $\text{cm d}^{-1}$ , with a median ice production is  $28 \text{ cm d}^{-1}$ . The highest ice production estimate occurred  
606 at CTD 35, closest to the Antarctic coastline and the Nansen Ice Shelf. The next largest value is  
607  $110 \text{ cm d}^{-1}$ , suggesting the ice production at CTD 35 is an outlier, and may have been influenced  
608 by platelet ice in upwelling ice shelf water that originated beneath the Nansen Ice Shelf  
609 (Robinson et al., 2014). In case there is an ice shelf water influence recorded in CTD 35, it will  
610 be excluded from the remainder of this analysis.

611           The remaining ice production rates span a range from 3 to 110 cm d<sup>-1</sup> and reveal some  
612 spatial and temporal trends that correspond with the varying conditions in different sectors of the  
613 TNBP. A longitudinal gradient emerges along the length of the polynya, when observing a  
614 subset of stations, categorized by similar wind conditions CTD 30 ( $U_{10}=11.50$  m s<sup>-1</sup>), CTD 27  
615 ( $U_{10}=10.68$  m s<sup>-1</sup>), and CTD 25 ( $U_{10}=11.77$  m s<sup>-1</sup>). Beginning upstream near the Nansen Ice  
616 shelf (Station 30) and moving downstream along the predominant wind direction toward the  
617 northeast, the ice production rate decreases. The upstream production rate is 63 cm d<sup>-1</sup> followed  
618 by midstream values of 28 cm d<sup>-1</sup>, and lastly downstream values of 14 cm d<sup>-1</sup>.

619           The spatial trend we observed somewhat mimics the 3D model of TNBP from Gallee  
620 (1997). During a four-day simulation, Gallee found highest ice production rates near the coast of  
621 50 cm d<sup>-1</sup>, and decreased to 0 cm d<sup>-1</sup> downstream and at the outer boundaries, further west than  
622 PIPERS Station 33 (Figure 10). Some of the individual ice production rates derived from  
623 PIPERS CTD profiles (e.g. 110 cm d<sup>-1</sup>) appear quite large compared to previous estimates,  
624 however it is worth emphasizing the dramatically different timescale that applies to these  
625 estimates. These “snapshots”, which capture ice production on the scale of tens of minutes, are  
626 more likely to capture the high frequency variability in this ephemeral process. As the katabatic  
627 winds oscillate, the polynyas enter periods of slower ice production, driving average rates down.  
628 To produce a comparable estimate, we attempt to scale these results to a seasonal average in the  
629 next section.

630



632

633

634

635

636

637

638

639

Figure 10: TNBP map of ice production rates. Map of TNBP CTD stations with anomalies and ice production rates. The CTD station number is listed in to the north of the stations. Listed inside the circle in black is the respective ice production rate in  $\text{cm d}^{-1}$ . The symbols and station numbers are colored by wind speed: Green indicates wind speeds less than  $10 \text{ m s}^{-1}$  (Stations 28, 29, 33, 34, 35), Orange indicates wind speeds between  $10$  and  $15 \text{ m s}^{-1}$  (Stations 25, 27, 30), and Red indicated wind speeds over  $15 \text{ m s}^{-1}$  (Station 32).



640

641 Table 2: Summary of mass of ice derived from salinity, lifetime, and production rates.

Station	$C_{ice}^S$ ( $\text{kgm}^{-3}$ )	$z_s$ (m)	$L_{M-0}$ (m)	$\varepsilon$ ( $\text{m}^2 \text{s}^{-3}$ )	MLD (m)	$t$ (min)	$r_{ice}$ ( $\text{cm d}^{-1}$ )	$r_{ice}$ 95% CI ( $\text{cm d}^{-1}$ )
25	$67 \times 10^{-3}$	13.4	141	$9.648 \times 10^{-5}$	350	9.8	14	[10-20]
26*	--	--	--	$7.191 \times 10^{-5}$	100	---	---	--
27	$46 \times 10^{-3}$	41.2	151	$8.188 \times 10^{-5}$	500	10.9	28	[20-37]
28	$21 \times 10^{-3}$	17.5	54	$1.622 \times 10^{-5}$	600	9.4	6	[4-10]
29	$51 \times 10^{-3}$	21.6	80	$5.375 \times 10^{-5}$	275	8.2	21	[15-28]
30	$105 \times 10^{-3}$	36	83	$3.771 \times 10^{-5}$	500	9.5	63	[45-88]
32	$119 \times 10^{-3}$	47	198	$3.466 \times 10^{-4}$	375	8.0	110	[67-81]
33	$29 \times 10^{-3}$	23.7	98	$2.844 \times 10^{-5}$	500	11.6	9	[5-13]
34	$89 \times 10^{-3}$	19.6	66	$6.397 \times 10^{-5}$	175	6.8	31	[23-42]
35	$266 \times 10^{-3}$	14.4	6	$2.343 \times 10^{-5}$	150	2.0	302	[200-456]
40	$13 \times 10^{-3}$	18.6	175	$9.603 \times 10^{-5}$	120	11.7	3	[2-5]

642 \*Station 26 did not have a measurable salinity anomaly but was included due to the clarity of the  
643 temperature anomaly. The term MLD stands for estimated mixed layer depth.

644

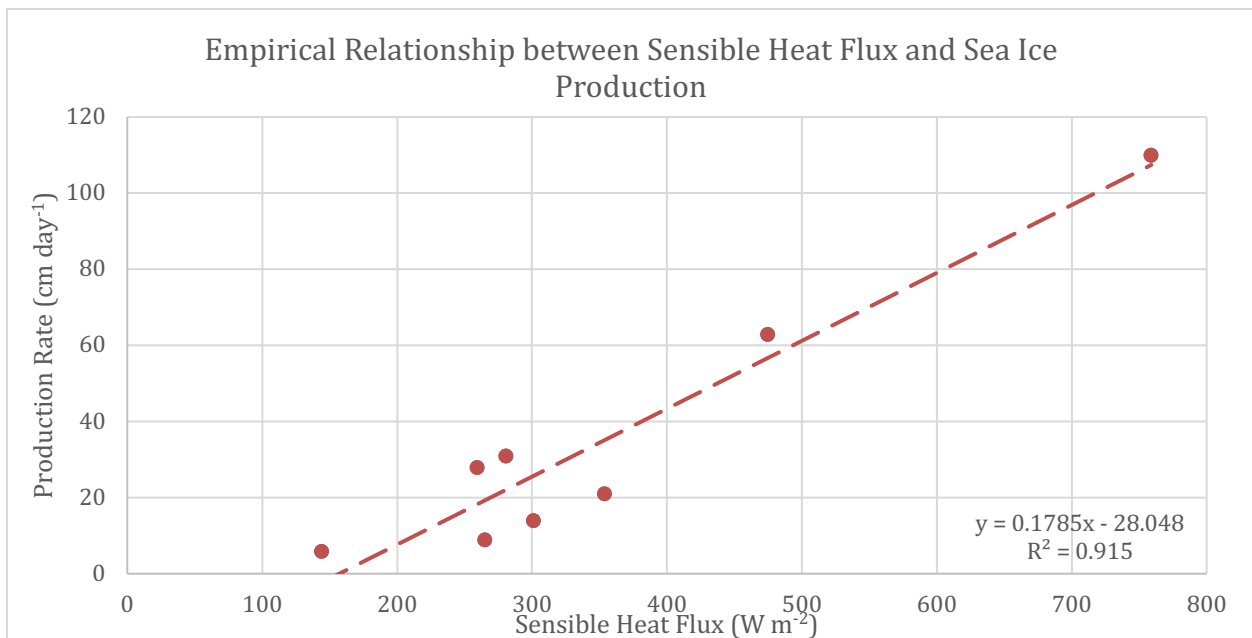
### 645 6.1 Seasonal Ice Production

646 We estimate the seasonal average in sea ice production by relating these in-situ ice  
647 production estimates to the time series atmospheric forcing from the automated weather stations,  
648 which extend over the season. The sensible heat flux ( $Q_s$ ) is used as a diagnostic term to  
649 empirically scale the ice production rates for the season;

650  $Q_s = C_p^A \rho_a C_s u_{10} (T_b - T_a) .$  (14)

651 Here  $C_p^A = 1.003 \text{ kJ kg}^{-1} \text{ K}^{-1}$ , the specific heat capacity of air at  $-23 \text{ }^\circ\text{C}$ ,  $C_s = 1.297 \times 10^{-3}$ , is the  
 652 heat transfer coefficient calculated using the COARE 3.0 code (Fairall et al, 2003). The values  
 653 are included in Supplemental Table S6.

654 First, the sensible heat flux was calculated at each TNBP CTD station using the  
 655 coincident NB Palmer meteorological data. Station 35 (see §5.1) and Station 40, in the Ross Sea  
 656 Polynya, were excluded from this calculation. Figure 11 depicts the trend between  $Q_s$  and sea ice  
 657 production rate; the high degree of correlation ( $R^2 = 0.915$ ) likely occurs because the same NB  
 658 Palmer wind speeds were used in the calculation of both  $Q_s$  and sea ice production (equation 7);  
 659 in other words, the two terms are not strictly independent of each other.



660  
 661 Figure 11: Empirical relationship between sensible heat flux and sea ice production: Production  
 662 rate =  $0.1785 Q_s - 28.048$ ,  $R^2$  of 0.915.

663  
 664 Next, the empirical trend was applied to a time series of  $Q_s$  from Station Manuela. The  
 665 met data from the NB Palmer and from Station Manuela (Figure 3) reveal that TNBP  
 666 experiences slower wind speeds and warmer temperatures than Station Manuela. This  
 667 phenomenon has been explained as a consequence of adiabatic warming and a reduction in the  
 668 topographic ‘Bernoulli’ effects that cause wind speed to increase at Station Manuela (Schick,  
 669 2018). Before applying the time series of met data from Manuela to equation (14) to calculate  $Q_s$ ,  
 670 we need to account for the offset. On average, the air temperatures were  $6.5 \text{ }^\circ\text{C}$  warmer, and

671 wind speed was on  $7.5 \text{ m s}^{-1}$  slower in TNB, during the 13 days that the vessel was in the  
672 polynya. Figure S6 shows the corrected data against the original data for the time in TNB.

673 We estimated the seasonal average in  $Q_s$  over TNBP using the corrected met data from  
674 Station Manuela, and an average sea surface temperature from the CTD stations ( $-1.91 \text{ }^\circ\text{C}$ ), the  
675 air density, specific heat capacity, and heat transfer coefficient remained the same as above.  
676 The average in  $Q_s$  from April to September is  $321 \text{ W m}^{-2}$ . Using the empirical relationship  
677 described in Figure 11, the seasonal average of frazil ice production in Terra Nova Bay polynya  
678 is  $29 \text{ cm d}^{-1}$ .

679 The seasonal sea ice production rate varies based on many factors affecting the rate of  
680 heat loss from the surface ocean. These factors include a strong negative feedback between  
681 ocean heat loss and sea ice cover. As the polynya builds up with ice, heat fluxes to the  
682 atmosphere will decline (Ackley et al, 2020) until that ice cover is swept out of the polynya by  
683 the next katabatic wind event. This spatial variation in ice cover and wind speed, produces strong  
684 spatial gradients in the heat loss to the atmosphere that drives ice production. For example,  
685 Ackley et al (2020) observed heat flux variations from nearly  $2000 \text{ W m}^{-2}$  to less than  $100 \text{ W m}^{-2}$   
686 over less than 1 km. An integrated estimate of total polynya sea ice production should take these  
687 spatial gradients and the changes in polynya area into account. That analysis is somewhat beyond  
688 the scope of this study, but we anticipate including these ice production estimates within  
689 forthcoming sea ice production estimates for 2017 and PIPERS.

690 One interesting outcome of the scaling relationship in Figure 11, is the value of the y-  
691 intercept at  $157 \text{ W m}^{-2}$ . This relationship suggests that frazil ice production ceases when the heat  
692 flux falls below this range. This lower bound, in combination with the spatial gradients in heat  
693 flux may help to establish the region where active production is occurring.

694

## 695 **6.2 Comparison to prior model and field estimates of ice production**

696 The seasonal average ice production of  $29 \text{ cm d}^{-1}$  estimated here, falls within the upper  
697 range of other in-situ ice production estimates. Schick (2018) estimated a seasonal average ice  
698 production rate of  $15 \text{ cm d}^{-1}$ , and Kurtz and Bromwich (1985), determined  $30 \text{ cm d}^{-1}$ . Both  
699 studies derived their ice production rates using a heat budget.

700 Overall, the ice production estimates from in-situ data, including heat flux estimates, are  
701 larger than the seasonal ice production estimates derived from remote sensing products. Drucker

702 et al (2011) used the AMSR-E instrument to obtain a seasonal average of 12 cm d<sup>-1</sup> for years  
703 2003-2008. Oshima et al, (2016) estimated 6 cm d<sup>-1</sup> of seasonal production for the years 2003-  
704 2011, and Nihashi and Ohshima (2015) determined 7 cm d<sup>-1</sup> for years 2003-2010. Finally,  
705 Tamura et al (2016) found production rates that ranged from 7-13 cm d<sup>-1</sup>, using both ECMWF  
706 and NCEP Reanalysis products for 1992-2013, reflecting a greater degree of consistency in  
707 successive estimates, likely because of consistency in the estimation methods.

708 Using a sea ice model, Sansiviero et al (2017) estimated seasonal average production of  
709 27 cm d<sup>-1</sup>, which falls closer to the estimates from in-situ measurements. Petrelli et al (2008)  
710 modeled an average daily rate of production of 14.8 cm d<sup>-1</sup> in the active polynya, using a coupled  
711 atmospheric-sea ice model. Fusco et al (2002) applied a model for latent heat polynyas and  
712 estimated a seasonal average production rate of 34 cm d<sup>-1</sup> for 1993 and 29 cm d<sup>-1</sup> for 1994, which  
713 is comparable to the in-situ budgets.

714

## 715 7. CONCLUSIONS

716 Polynyas have been regarded as ice production factories, which are responsible for total  
717 volumetric ice production that is vastly disproportionate to their surface area. This study  
718 documented temperature and salinity anomalies in the upper ocean that reflect vigorous frazil ice  
719 production in polynyas. These anomalies produce an unstable water column that can be  
720 observed as a quasi-stationary feature in the density profile. The only comparable example is  
721 found in the outflow of supercooled ice shelf waters, which occur much deeper in the water  
722 column. These features were observed during strong katabatic wind events in the Terra Nova  
723 Bay and the Ross Sea polynyas, with ocean heat losses to the atmosphere in excess of 2000 W m<sup>-2</sup>.  
724 The anomalies provide additional insights into the ice production within polynyas, and have  
725 provided estimates of frazil ice production rates, in-situ. The frazil production rates varies from 3  
726 to 110 cm d<sup>-1</sup>, with a seasonal average of 29 cm d<sup>-1</sup>, and the method captures ice production on  
727 the timescale of minutes to tens of minutes, which is significantly shorter than the more common  
728 daily or monthly production rates.

729 These estimates may suggest that frazil ice is a more significant ice type for ice  
730 production in polynyas, than was previously thought. However, it is not clear how many frazil  
731 ice crystals survive to become part of the consolidated seasonal ice pack. In this vigorous mixing

732 environment, a fraction may melt and become reincorporated into the ocean, before they have a  
733 chance to aggregate.

734 By the same token, frazil production and the estimates of ice production could be  
735 improved by collecting consecutive CTD casts at the same location, to observe how these  
736 anomalies evolve on the minute-to-minute timescale, which can be challenging in regions of  
737 active ice formation. One exciting outcome of this study is the suggestion that it is possible to  
738 obtain synoptic inventories of ice production. For example, a float or glider that measures  
739 surface CTD profiles on a frequent basis, would improve our synoptic and seasonal  
740 understanding of polynya ice production as they respond to annual and secular modes of the  
741 ocean and atmosphere.

742

743

## 744 **8. REFERENCES**

745

746 Ackley, S.F., Stammerjohn, S., Maksym, T. Smith, M., Cassano, J., Guest P. Tison, J-L.,  
747 Delille, B. Loose, B., Sedwick, P. DePace, L., Roach, L., Parno, J. Sea ice production  
748 and air-ice-ocean-biogeochemistry interactions in the Ross Sea during the PIPERS  
749 2017 autumn field campaign, *Ann. Glaciol.*, 2020 in review.

750 Armstrong, T.: World meteorological organization: wmo sea-ice nomenclature.

751 terminology, codes and illustrated glossary, *J. Glaciol.*, 11, 148-149, [https://doi-](https://doi-org.uri.idm.oclc.org/10.3189/S0022143000022577)  
752 [org.uri.idm.oclc.org/10.3189/S0022143000022577](https://doi-org.uri.idm.oclc.org/10.3189/S0022143000022577), 1972.

753 Bromwich, D. H., and Kurtz, D. D.: Katabatic wind forcing of the terra nova bay polynya, *J.*

754 *Geophys. Res.*, 89, 3561-3572, [https://doi-](https://doi-org.uri.idm.oclc.org/10.1029/JC089iC03p03561)

755 [org.uri.idm.oclc.org/10.1029/JC089iC03p03561](https://doi-org.uri.idm.oclc.org/10.1029/JC089iC03p03561), 1984.

756 Buffoni, G., Cappelletti, A., and Picco, P.: An investigation of thermohaline circulation in

757 terra nova bay polynya, *Antarct. Sci.*, 14.1, 83-92, [https://doi-](https://doi-org.uri.idm.oclc.org/10.1017/S0954102002000615)

758 [org.uri.idm.oclc.org/10.1017/S0954102002000615](https://doi-org.uri.idm.oclc.org/10.1017/S0954102002000615), 2002.

759 Cosimo J.C., and Gordon A.L.: Inter-annual variability in summer sea ice minimum,

760 coastal polynyas and bottom water formation in the weddell sea, in: *Antarctic sea ice:*

761 *physical processes, interactions and variability*, 74, edited by: Jeffries, M.O., American

762 Geophysical Union, Washington, D.C., 293-315, <https://doi.org/10.1029/AR074p0293>,  
763 1998.

764 Cox, G. F. N., and Weeks, W. F.: Equations for determining the gas and brine volumes in  
765 sea-ice samples, *J. Glaciol.*, 29, 306-316, <https://doi.org/10.3189/S0022143000008364>,  
766 1983.

767 Cushman-Roisin, B.: *Environmental Fluid Mechanics*, John Wiley & Sons, New York,  
768 2019.

769 Dmitrenko, I. A., Wegner, C., Kassens, H., Kirillov, S. A., Krumpen, T., Heinemann, G.,  
770 Helbig, A., Schroder, D., Holemann, J.A., Klagger, T., Tyshko, K.P., and Busche, T.:  
771 Observations of supercooling and frazil ice formation in the laptev sea coastal polynya,  
772 *J. Geophys. Res.*, 115, <https://doi-org.uri.idm.oclc.org/10.1029/2009JC005798>, 2010.

773 Drucker, R., S. Martin, and R. Kwok: Sea ice production and export from coastal polynyas  
774 in the Weddell and Ross Seas. *Geophys. Res. Lett.*, 38, L17502,  
775 <https://doi.org/10.1029/2011GL048668m>, 2011.

776 Fairall, C.W., Bradley, E.F., Hare, J.E., Grachev, A.A., and Edson, J.B.:  
777 Bulk parameterization of air sea fluxes: updates and verification for the COARE  
778 algorithm, *J. Climate*, 16, 571-590, [https://doi.org/10.1175/1520-0442\(2003\)016<0571:BPOASF>2.0.CO;2](https://doi.org/10.1175/1520-0442(2003)016<0571:BPOASF>2.0.CO;2), 2003.

780 Fetterer, F., K. Knowles, W. N. Meier, M. Savoie, and A. K. Windnagel. 2017, updated  
781 daily. *Sea Ice Index, Version 3*. Sea Ice Index, Version 3. Boulder, Colorado USA.  
782 NSIDC: National Snow and Ice Data Center. <https://doi.org/10.7265/N5K072F8>. 09  
783 March 2019.

784 Fusco, G., Flocco, D., Budillon, G., Spezie, G., and Zambianchi, E.: Dynamics and  
785 variability of terra nova bay polynya, *Marine Ecology*, 23, 201–209,  
786 <https://doi.org/10.1111/j.1439-0485.2002.tb00019.x>, 2002.

787 Fusco, G., Budillon, G., and Spezie, G.: Surface heat fluxes and thermohaline variability in  
788 the ross sea and in terra nova bay polynya, *Cont. Shelf Res.*, 29(15), 1887-1895.  
789 <https://doi.org/10.1016/j.csr.2009.07.006>, 2009.

790 Gallée, H.: Air-sea interactions over terra nova bay during winter: simulation with a  
791 coupled atmosphere-polynya model, *J. Geophys. Res-Atmos.*, 102, 13835–13849,  
792 <https://doi.org/10.1029/96JD03098>, 1997.

793 Heorton, H. D. B. S., Radia, N., and Feltham, D. L.: A model of sea ice formation in leads  
794 and polynyas, *J. Phys. Oceanogr.*, 47, 1701-1718, [https://doi.org/10.1175/JPO-D-16-](https://doi.org/10.1175/JPO-D-16-0224.1)  
795 0224.1, 2017.

796 Ito, M., Ohshima, K., Fukamachi, Y., Simizu, D., Iwamoto, K., Matsumura, Y., Eicken, H.:  
797 Observations of supercooled water and frazil ice formation in an Arctic coastal  
798 polynya from moorings and satellite imagery, *Ann. Glaciol.*, 56, 307-314,  
799 <https://doi.org/10.3189/2015AoG69A839>, 2015.

800 Jacobs, S. S.: Bottom water production and its links with the thermohaline circulation,  
801 *Antarct. Sci.*, 16, 427-437, <https://doi.org/10.1017/S095410200400224X>, 2004.

802 Knuth, M. A. and Ackley, S. F.: Summer and early-fall sea-ice concentration in the ross  
803 sea: comparison of in situ ASPeCt observations and satellite passive microwave  
804 estimates, *Ann. Glaciol.*, 44, 303-309, <https://doi.org/10.3189/172756406781811466>,  
805 2006.

806 Kurtz, D. D. and Bromwich, D. H.: A recurring, atmospherically forced polynya in terra  
807 nova bay in *Antarctic Research Series*, 43, edited by: Jacobs, S.S., 43, American  
808 Geophysical Union, Washington, D.C., 177-201, <https://doi.org/10.1029/AR043p0177>,  
809 1985.

810 Lombardo, C., and Gregg, M.: Similarity scaling of viscous and thermal dissipation in a  
811 convecting surface boundary layer., *J. Geophys. Res.*, 94, , 6273-6284.  
812 <https://doi.org/10.1029/JC094iC05p06273>, 1989.

813 Manwell, J. F., McGowan, J. G., and Rogers, A. L. *Wind energy explained: theory, design*  
814 *and application*. John Wiley & Sons, West Sussex, England,  
815 <https://doi.org/10.1002/9781119994367>, 2010.

816 Martin, S.: Frazil ice in rivers and oceans, *Annu. Rev. Fluid Mech.*, 13(1), 379-397.  
817 <https://doi.org/10.1146/annurev.fl.13.010181.002115>, 1981.

818 Martin, S., Drucker, R. S., and Kwok, R.: The areas and ice production of the western and  
819 central ross sea polynyas, 1992-2002, and their relation to the B-15 and C-19 iceberg  
820 events of 2000 and 2002, *J. Marine Syst.*, 68, 201-214,  
821 <https://doi.org/10.1016/j.jmarsys.2006.11.008>, 2007.

822 Mathiot, P., Jourdain, N., Barnier, C., Gallée, B., Molines, H., Sommer, J., and Penduff,  
823 M.: Sensitivity of coastal polynyas and high-salinity shelf water production in the Ross

824 Sea, antarctica, to the atmospheric forcing, *Ocean Dynam.*, 62(5), 701-723,  
825 <https://doi.org/10.1007/s10236-012-0531-y>, 2012.

826 Matsumura, Y., and Ohshima, K. I.: Lagrangian modelling of frazil ice in the ocean, *Ann.*  
827 *Glaciol.*, 56(69), 373–382, <https://doi.org/10.3189/2015AoG69A657>, 2017.

828 Michel, B.: Physics of snow and ice: morphology of frazil ice, International Conference on  
829 Low Temperature Science. I, Conference on Physics of Snow and Ice, II, Conference  
830 on Cryobiology, Sapporo, Japan, 14-19 August 1966, Sapporo, Japan, 119–128, 1967.

831 Monin, A. S., and Obukhov, A. M.: Basic laws of turbulent mixing in the surface layer of  
832 the atmosphere, *Contrib. Geophys. Inst. Acad. Sci. USSR*, 24, 163-187, 1954.

833 Morales Maqueda, M. A., Willmott, A. J., and Biggs, N. R. T.: Polynya dynamics: a  
834 review of observations and modeling, *Rev. Geophys.*, 42(1), RG1004,  
835 <https://doi.org/10.1029/2002RG000116>, 2004.

836 Nelson, M., Queste, B., Smith, I., Leonard, G., Webber, B., & Hughes, K.: Measurements  
837 of Ice Shelf Water beneath the front of the Ross Ice Shelf using gliders, *Ann. Glaciol.*,  
838 58(74), 41-50. doi:10.1017/aog.2017.34, 2017.

839 Nihashi, S. and K.I. Ohshima: Circumpolar mapping of Antarctic coastal polynyas and  
840 landfast sea ice: relationship and variability. *J. Climate*, 28, 3650-3670,  
841 <https://doi.org/10.1175/JCLI-D-14-00369.1> 2015.

842 Orsi, A.H. and Wiederwohl, C.L.: A recount of Ross Sea waters, *Deep-Sea Res. Pt. II*,  
843 56(13), 778-795, <https://doi.org/10.1016/j.dsr2.2008.10.033>, 2009.

844 Ohshima, K.I., Nihashi, S. & Iwamoto, K. Global view of sea-ice production in polynyas  
845 and its linkage to dense/bottom water formation. *Geosci. Lett.* 3, 13,  
846 <https://doi.org/10.1186/s40562-016-0045-4>, 2016.

847 Ozsoy-Cicek, B., Xie, H., Ackley, S. F., and Ye, K.: Antarctic summer sea ice concentration  
848 and extent: comparison of ODEN 2006 ship observations, satellite passive microwave  
849 and NIC sea ice charts, *The Cryosphere*, 3(1), 1-9, <https://doi.org/10.5194/tc-3-1-2009>,  
850 2009.

851 Park, J., Kim, H.-C., Jo, Y.-H., Kidwell, A., and Hwang, J.: Multi-temporal variation of the  
852 ross sea polynya in response to climate forcings, *Polar Res.*, 37(1),  
853 <https://doi.org/10.1080/17518369.2018.1444891>, 2018.



854 Petrelli, P., Bindoff, N. L., and Bergamasco, A.: The sea ice dynamics of terra nova bay and  
855 ross ice shelf polynyas during a spring and winter simulation, *J. Geophys. Res.-*  
856 *Oceans*, 113(C9), <https://doi.org/10.1029/2006JC004048>, 2008.

857 Robinson, N. J., Williams, M. J., Stevens, C. L., Langhorne, P. J., and Haskell, T.  
858 G.: Evolution of a supercooled ice shelf water plume with an actively growing subice  
859 platelet matrix, *J. Geophys. Res.-Oceans*, 119(6), 3425-3446,  
860 <https://doi.org/10.1002/2013JC009399>, 2014.

861 Robinson, N.J., Grant, B.S, Stevens, C.L., Stewart, C.L., Williams, M.J.M. Oceanographic  
862 observations in supercooled water: Protocols for mitigation of measurement errors in  
863 profiling and moored sampling, *Cold Regions Science and Technology*, 170,  
864 <https://doi.org/10.1016/j.coldregions.2019.102954>, 2020.

865 Sansiviero, M., Morales Maqueda, M. Á., Fusco, G., Aulicino, G., Flocco, D., and Budillon,  
866 G.: Modelling sea ice formation in the terra nova bay polynya, *J. Marine Syst.*, 166, 4–  
867 25, <https://doi.org/10.1016/j.jmarsys.2016.06.013>, 2017.

868 SBE 911plus CTD- SBE 911plus CTD Datasheet: [https://www.seabird.com/profiling/sbe-](https://www.seabird.com/profiling/sbe-911plus-ctd/family-downloads?productCategoryId=54627473769)  
869 [911plus-ctd/family-downloads?productCategoryId=54627473769](https://www.seabird.com/profiling/sbe-911plus-ctd/family-downloads?productCategoryId=54627473769), 15 August 2018,  
870 2016.

871 Schick, K. E.: Influences of Weather and Surface Variability on Sensible Heat Fluxes in  
872 Terra Nova Bay, Antarctica,  
873 [https://scholar.colorado.edu/concern/graduate\\_thesis\\_or\\_dissertations/m613mx873](https://scholar.colorado.edu/concern/graduate_thesis_or_dissertations/m613mx873),  
874 2018.

875 Skogseth, R., Nilsen, F., and Smedsrud, L. H.: Supercooled water in an Arctic polynya:  
876 observations and modeling, *J. Glaciol.*, 55(189), 43–52,  
877 <https://doi.org/10.3189/002214309788608840>, 2009.

878 Smith, M., and Thomson, J.: Ocean surface turbulence in newly formed marginal ice zones,  
879 *J. Geophys. Res.-Oceans*, 124(3), 1382-1398, <https://doi.org/10.1029/2018JC014405>,  
880 2019.

881 Talley, L.D., Picard, G.L., Emery, W.J. Swift, J.H.: Descriptive physical oceanography: an  
882 introduction, 6, Academic Press, Elsevier, Boston, 2011.

883 Tamura, T., Ohshima, K. I., and Nihashi, S.: Mapping of sea ice production for Antarctic  
884 coastal polynyas, *Geophys. Res. Lett.*, 35(7), 1–5,  
885 <https://doi.org/10.1029/2007GL032903>, 2008.

886 Tamura, T., K. I. Ohshima, A. D. Fraser and G. D. Williams: Sea ice production variability  
887 in Antarctic coastal polynyas, *J. Geophys. Res.*, 121, 2967–2979,  
888 <https://doi.org/10.1002/2015JC011537>, 2016.

889 Thomson, J.: Wave breaking dissipation observed with “swift” drifters, *J. Atmos. Ocean*  
890 *Tech.*, 29(12), 1866–1882, <https://doi.org/10.1175/JTECH-D-12-00018.1>, 2012.

891 Thomson, J., Schwendeman, M., and Zippel, S. Wave-breaking turbulence in the ocean  
892 surface layer., *J. Phys. Oceanogr.*, 46, 1857–1870, [https://doi.org/10.1175/JPO-D-15-](https://doi.org/10.1175/JPO-D-15-0130.1)  
893 [0130.1](https://doi.org/10.1175/JPO-D-15-0130.1), 2016.

894 Ushio S., and Wakatsuchi, M.: A laboratory study on supercooling and frazil ice production  
895 processes in winter coastal polynyas, *J. Geophys. Res.-Oceans*, 98(C11), 20321–  
896 20328, <https://doi.org/10.1029/93JC01905>, 1993.

897 Van Woert, M. L.: The wintertime expansion and contraction of the terra nova bay polynya,  
898 *Oceanography of the Ross Sea: Antarctica*, Spezie, G. and Manzella, G. M. R.,  
899 Springer, Milano, 145–164, [https://doi.org/10.1007/978-88-470-2250-8\\_10](https://doi.org/10.1007/978-88-470-2250-8_10), 1999a.

900 Van Woert, M. L.: Wintertime dynamics of the terra nova bay polynya, *J. Geophys. Res.*,  
901 104, 7753–7769, <https://doi.org/10.1029/1999JC900003>, 1999b.

902 Vallis, G.: Atmospheric and oceanic fluid dynamics: fundamentals and large-scale  
903 circulation. Cambridge: Cambridge University Press,  
904 <https://doi.org/10.1017/9781107588417>, 2017.

905 Weissling, B., Ackley, S., Wagner, P., and Xie, H.: EISCAM — Digital image acquisition  
906 and processing for sea ice parameters from ships, *Cold Reg. Sci. Technol.*, 57(1), 49–  
907 60, <https://doi.org/10.1016/j.coldregions.2009.01.001>, 2009.

908 Wilchinsky, A. V., Heorton, H. D. B. S., Feltham, D. L., and Holland, P. R.: Study of the  
909 impact of ice formation in leads upon the sea ice pack mass balance using a new frazil  
910 and grease ice parameterization, *J. Phys. Oceanogr.*, 45(8), 2025–2047,  
911 <https://doi.org/10.1175/JPO-D-14-0184.1>, 2015.

912 Worby, A. P., Geiger, C. A., Paget, M. J., Van Woert, M. L., Ackley, S. F., and DeLiberty,  
913 T. L.: Thickness distribution of antarctic sea ice. *J. Geophys. Res. - Oceans*, 113(C5),  
914 <https://doi.org/10.1029/2007JC004254>, 2008.

915 Zhang, G.: A further study on estimating surface evaporation using monthly mean data:  
916 comparison of bulk formulations, *J. Climate*, 10(7), 1592-1600,  
917 [https://doi.org/10.1175/1520-0442\(1997\)010%3C1592:AFSOES%3E2.0.CO;2](https://doi.org/10.1175/1520-0442(1997)010%3C1592:AFSOES%3E2.0.CO;2), 1997.

918 Zippel, S. F., and Thomson, J. (2016). Air-sea interactions in the marginal ice zone.  
919 *Elementa Science of the Anthropocene*, 4, 95,  
920 <http://doi.org/10.12952/journal.elementa.000095>, 2016.

921

922

## 923 8. ACKNOWLEDGEMENTS

924 We thank Pat Langhorne and one anonymous reviewer for their insightful comments and  
925 corrections that have improved this manuscript. This work was supported by the National  
926 Science Foundation through NSF Award Nos 1744562 (B. Loose, L. de Pace, URI); 134717  
927 (S.F. Ackley, UTSA); 1341513 (E. Maksym, WHOI);1341725 (P.Guest, NPS); 1341606 (S.  
928 Stammerjohn and J. Cassano, U Colo). This work was also supported by the National  
929 Atmospheric and Space Administration through NASA Grant No 80NSSC19M0194 (S. F.  
930 Ackley) to the Center for Advanced Measurements in Extreme Environments at UTSA. The  
931 authors appreciate the support of the University of Wisconsin-Madison Automatic Weather  
932 Station Program for the data set, data display, and information.

933

## 934 9. DATA AVAILABILITY

935

936 The data used in this publication are publicly available from the US Antarctic Program Data  
937 Center <http://www.usap-dc.org/view/dataset/601192> and through the CLIVAR Carbon and  
938 Hydrographic Data Office <https://cchdo.ucsd.edu/cruise/320620170410>.

939

940

## 941 10. AUTHOR CONTRIBUTIONS

942

943 LD prepared the manuscript and carried out analyses. MS and JT provided SWIFT data and  
944 guidance for upper ocean turbulence analysis. SS prepared and processed the PIPERS CTD data  
945 and provided water mass insights during manuscript preparation; SA lead the PIPERS expedition  
946 and supported ice interpretations. BL participated in PIPERS expedition, inferred possibility of  
947 frazil ice growth and advised LD during manuscript preparation.

948

## 949 11. COMPETING INTERESTS

950

951 The authors declare that they have no conflict of interest.